AFRL-RV-HA-TR-2009-1023

Developments of Finite-Frequency Seismic Theory and Applications to Regional Tomographic Imaging

Yang Shen
Xiaoping Yang

Science Applications International Corporation
4001 N. Fairfax Dr.
Arlington, VA 22209

Final Report

31 January 2009

APPROVED FOR PUBLIC RELEASE; DISTRIBUTION UNLIMITED.

AIR FORCE RESEARCH LABORATORY
Space Vehicles Directorate
29 Randolph Rd
AIR FORCE MATERIEL COMMAND
HANSCOM AFB, MA 01731-3010

NOTICES

Using Government drawings, specifications, or other data included in this document for any purpose other than Government procurement does not in any way obligate the U.S. Government. The fact that the Government formulated or supplied the drawings, specifications, or other data does not license the holder or any other person or corporation; or convey any rights or permission to manufacture, use, or sell any patented invention that may relate to them.

This report was cleared for public release and is available to the general public, including foreign nationals. Qualified requestors may obtain additional copies from the Defense Technical Information Center (DTIC) (http://www.dtic.mil). All others should apply to the National Technical Information Service.

AFRL-RV-HA-TR-2009-1023 HAS BEEN REVIEWED AND IS APPROVED FOR PUBLICATION IN ACCORDANCE WITH ASSIGNED DISTRIBUTION STATEMENT.

//Signature//	//Signature//
ROBERT J. RAISTRICK Contract Manager	PAUL TRACY, Acting Chief Battlespace Surveillance Innovation Center

This report is published in the interest of scientific and technical information exchange, and its publication does not constitute the Government's approval or disapproval of its ideas or findings.

REPORT DOCUMENTATION PAGE

Form Approved
OMB No. 0704-0188

Public reporting burden for this collection of information is estimated to average 1 hour per response, including the time for reviewing instructions, searching existing data sources, gathering and maintaining the data needed, and completing and reviewing this collection of information. Send comments regarding this burden estimate or any other aspect of this collection of information, including suggestions for reducing this burden to Department of Defense, Washington Headquarters Services, Directorate for Information Operations and Reports (0704-0188), 1215 Jefferson Davis Highway, Suite 1204, Arlington, VA 22202-4302. Respondents should be aware that notwithstanding any other provision of law, no person shall be subject to any penalty for failing to comply with a collection of information if it does not display a currently valid OMB control number. **PLEASE DO NOT RETURN YOUR FORM TO THE ABOVE ADDRESS.**

1. REPORT DATE *(DD-MM-YYYY)* 31-January-2009	**2. REPORT TYPE** Final Report	**3. DATES COVERED** *(From - To)* 04-07-2005 to 12-31-2008

4. TITLE AND SUBTITLE
Developments of Finite-Frequency Seismic Theory and Applications to Regional Tomographic Imaging

5a. CONTRACT NUMBER
FA8718-05-C-0017

5b. GRANT NUMBER

5c. PROGRAM ELEMENT NUMBER
1010

6. AUTHOR(S)
Yang Shen[1] and Xiaoping Yang

5d. PROJECT NUMBER
SM

5e. TASK NUMBER
A1

5f. WORK UNIT NUMBER

7. PERFORMING ORGANIZATION NAME(S) AND ADDRESS(ES)

Science Applications International Corporation,
4001 Fairfax Dr.
Arlington, VA 22209

8. PERFORMING ORGANIZATION REPORT NUMBER

9. SPONSORING / MONITORING AGENCY NAME(S) AND ADDRESS(ES)

Air Force Research Laboratory
29 Randolph Rd.
Hanscom AFB, MA 01731-3010

10. SPONSOR/MONITOR'S ACRONYM(S)
AFRL/RVBYE

11. SPONSOR/MONITOR'S REPORT NUMBER(S)
AFRL-RV-HA-TR-2009-1023

12. DISTRIBUTION / AVAILABILITY STATEMENT

Approved for Public Release; Distribution Unlimited.

13. SUPPLEMENTARY NOTES

[1] Graduate School of Oceanography, University of Rhode Island, South Ferry Rd., Narragansett, RI 02882

14. ABSTRACT

We use "banana-doughnut" sensitivity kernels of teleseismic body waves to image the crust and mantle beneath eastern Eurasia. We have collected and processed available broadband data from both permanent stations and temporary networks in eastern Eurasia. In southeast Tibet, where a PASSCAL experiment provided a dense station coverage, a detailed study is carried out to obtain high-resolution P- and S-velocity models. A regional P-wave velocity model for eastern Eurasia is also obtained by inverting the finite-frequency traveltimes of teleseismic body waves from available broadband stations in eastern Eurasia. To improve resolution in the crust and uppermost mantle, we have made several contributions to the finite-difference, scattering-integral method (FDSIM), including the finite-frequency sensitivity kernels for head waves and component-dependent sensitivities. We have also developed surface-wave tomography using the ambient seismic noise from 3D sensitivity kernels for finite-frequency Green's functions. We demonstrate that high-resolution tomographic models of the crust and upper mantle can be achieved using finite-frequency teleseismic body waves in places with dense stations, such as southeast Tibet. We show that the continental-scale P velocity model obtained from finite-frequency teleseismic body wave tomography is comparable to that of the high-resolution study in southeast Tibet.

15. SUBJECT TERMS
Seismic tomography, Seismic sensitivity kernels, Seismic velocity models

16. SECURITY CLASSIFICATION OF:			**17. LIMITATION OF ABSTRACT**	**18. NUMBER OF PAGES**	**19a. NAME OF RESPONSIBLE PERSON** Robert Raistrick
a. REPORT UNCLASSIFIED	**b. ABSTRACT** UNCLASSIFIED	**c. THIS PAGE** UNCLASSIFIED	SAR	48	**19b. TELEPHONE NUMBER** *(include area code)* 781-377-3726

Table of Contents

1. SUMMARY 1

2. INTRODUCTION 2

3. TECHNICAL APPROACH.. 2

    3.1 Finite-Frequency Tomography of Teleseismic Body Waves 2

        3.1.1 Finite-Frequency Traveltime Data 2

        3.1.2. P- and S-Velocity Models in Southeast Tibet 3

        3.1.3. P-velocity model of East Eurasia 4

    3.2. Finite-Frequency Sensitivity Kernels for Pn/Sn Waves 5

    3.3. Component-Dependent Sensitivity Kernels and Utility of Three-Component Seismic Records 5

    3.4. Finite-Frequency Ambient Noise Tomography 6

4. DISCUSSION AND CONCLUSIONS 7

5. RECOMMENDATIONS 8

REFERENCES 17

LIST OF SYSMOLS, ABBREVIATIONS, AND ACROYMS OF SYMBOLS............. 20

APPENDIX I. Frequency-Dependent Crustal Correction for Finite-Frequency Seismic Tomography by Ting Yang and Yang Shen

APPENDIX II. Finite Frequency Tomography in Southeastern Tibet by Yong Ren and Yang Shen

List of Figures

Figure 1 Topography of Eastern Eurasia and the distribution of broadband seismic stations 9

Figure 2 (a) P-velocity perturbations beneath southeastern Tibet. (b) S-velocity perturbations. (c) Cross-section A-B through P and S-wave tomographic models.. 10

Figure 3 The P-velocity variations relative to iasp91..........11

Figure 4 (a) The traveltime sensitivity kernels for the head wave recorded on the vertical component on the horizontal planes. (b) The traveltime sensitivity kernel for the head wave on a vertical profile half way between the source and receiver and perpendicular to the ray path. (c) The traveltime sensitivity kernels for the head wave on the vertical profile containing the source and receiver..........12

Figure 5 The kernels for the vertical component of head waves in the models with up-bending and down-bending layer interface between the source and receiver. (a) A cylindrical down-bending interface. (b) An up-bending interface..........13

Figure 6 Delay-time and amplitude sensitivity kernels for the z and x components and their differential kernel..........14

Figure 7 Cross-sections of phase-delay sensitivities to Vs perturbations between the vertical components of two seismic stations in southeast Tibet 15

Figure 8 Preliminary Vs perturbation models from the inversion of estimated Green’s function phase delays. 16

ACKNOWLEDGMENTS

We thank Dr. Bob Engdahl for the EHB catalog, Dr. Youshun Sun for the crust model in China, and the IRIS DMC and the National Research Institute for Earth Science and Disaster Prevention (Japan) for providing broadband seismic data. Dr. Ting Yang collected and processed most of finite-frequency body wave traveltime data from permanent stations in east Eurasia. Dr. Li Zhao played an important role in the development of the finite-difference, scattering-integral method (FDSIM). We also thank Kim Olsen for the staggered finite-difference code, which was used in the study of head waves and the component-dependent sensitivity kernels. This work would not be possible without the creativity and dedication of the students and postdocs directly or indirectly involved in the project (Zhigang Zhang, Dr. Yong Ren, and Dr. Wei Zhang).

1. SUMMARY

Recent advances in seismic theory have provided more accurate representation of the propagation of finite-frequency seismic waves than ray theory. In this project, we use the "banana-doughnut" sensitivity kernels of teleseismic body waves to image the crust and mantle beneath eastern Eurasia. We have collected and processed available broadband data from both permanent stations and temporary networks in eastern Eurasia. In southeast Tibet, where a PASSCAL experiment provided a dense station coverage, a detailed study is carried out to obtain high-resolution P- and S-velocity models, which provide not only important constraints on the continental collision and plateau building processes but also a reference for comparison with a larger regional-scale inversion. The P and S-wave velocity models reveal a low-velocity anomaly in the crust and upper mantle to ~ 300 km depth beneath a north-south-trending rift zone in southeastern Tibet. This low velocity anomaly is situated above a tabular, high-dipping-angle, high-velocity anomaly that extends into the upper mantle transition zone. These results are evidence for the delamination of the mantle lithosphere and its causal relationship to the formation of the north-south trending rift in southeastern Tibet. A regional P-wave velocity model for eastern Eurasia is also obtained by inverting the finite-frequency traveltimes of teleseismic body waves from available broadband stations in eastern Eurasia. In southeast Tibet, the regional model is quantitatively consistent with the results of the local and detailed study. Because of steep incidence of teleseismic body waves at shallow depth, gaps in resolution exist in the shallow upper mantle and crust in places with sparse stations.

In the crust and uppermost mantle, where the velocity structure is highly heterogeneous, a 1D reference model and single-scattering approximation may become invalid. To improve resolution in the crust and uppermost mantle, we have made several contributions to the finite-difference, scattering-integral method (FDSIM). These include the finite-frequency sensitivity kernels for head waves and component-dependent sensitivities due to uneven distribution of scattered waves on the different components of the same arrival. Furthermore, we apply the finite-frequency methodology to surface-wave tomography using the ambient seismic noise. Unlike previous studies that use estimated Green's functions to solve for phase or group velocity maps and then a point-wise S velocity structure under a 1D assumption, we construct 3D sensitivity kernels for the finite-frequency Green's functions, taking into account a 3D reference model and the effects of topographic variations. The sensitivity kernels and the phase delays between the estimated Green's functions and synthetics are inverted for Vp and Vs structure beneath southeast Tibet. Results show that the wave speed in the reference model (a modified CRUST 2.0) is too high in the lower crust and too low in the shallow crust beneath southeast Tibet.

2. INTRODUCTION

In seismic tomographic studies to date the reference models are commonly 1D and the structural sensitivity kernels of seismic data are calculated without considering the finiteness of seismic waves in both time and frequency domains. These simplifications result in a theoretical limit (Nolet and Dahlen, 2000; Baig et al., 2003), in addition to that from the data coverage, on the structural resolution that can be achieved in tomography. In recent years, seismologists have started to replace the great-circle path of a surface wave with sensitivity kernels having a finite width and symmetrically distributed across the great-circle path (e.g., Yoshizawa and Kennett, 2002; Ritzwoller et al., 2002) or a more physically realistic kernel calculated using 1D (e.g., Li and Romanowicz, 1996; Zhou et al., 2004, 2006) or 3D (e.g., Liu and Tromp, 2006; Shen et al., 2008b) reference models. Similarly, several studies (e.g., Hung et al., 2004; Montelli et al., 2004; 2006; Yang et al., 2006; Chen et al., 2007b; Sigloch et al., 2008; Ren and Shen, 2008) have replaced body-wave ray paths with "banana-doughnut" sensitivity kernels calculated in 1D (Dahlen et al., 2000; Hung et al., 2000; Zhao et al., 2000; Zhao and Jordan, 2006) or 3D (Tromp et al., 2005; Zhao et al., 2005; Liu and Tromp, 2006; Zhang et al., 2007) reference models.

The use of body wave ray theory, a 1D reference model, and Born single-scattering approximation makes it possible to calculate the sensitivity kernels of high frequency teleseismic body waves at a relatively low computational cost (Dahlen et al., 2000; Hung et al., 2000). On the other hand, computationally intensive numerical approaches such as the finite-difference or spectral-element method represent more accurately complex interactions of full waves in 3D heterogeneous media and make it possible to iteratively improve upon a 3D model.

In the following sections, we document our application of the "banana-doughnut" sensitivity kernels based on 1D reference models to teleseismic body-wave traveltime tomography in east Eurasia. We demonstrate that high-resolution tomographic models of the crust and upper mantle can be achieved using finite-frequency teleseismic body waves in places with dense stations, such as southeast Tibet. We show that the continental-scale P velocity model obtained from finite-frequency teleseismic body wave tomography is comparable to that of the high-resolution study in southeast Tibet. In order to improve resolution in the crust and uppermost mantle, we made several contributions to the full-wave tomography method based on finite-difference simulations of wave propagation in 3D reference models. We applied the full-wave approach to image the crust and upper mantle beneath southeast Tibet using ambient noise.

3. TECHNICAL APPROACH

3.1 Finite-Frequency Tomography of Teleseismic Body Waves

3.1.1 Finite-Frequency Traveltime Data

We collected and utilized available broadband waveforms to construct the finite-frequency velocity model beneath eastern Eurasia. Figure 1 shows the distribution of the stations, which include the Global Seismographic Network (GSN), Japanese F-net and JISNET, Taiwan Broadband Seismic Network, and other regional seismic networks available at the Data Management Center (DMC) of the Incorporated Research Institutions for Seismology (IRIS). We selected global earthquakes in the updated Engdahl-van der Hilst-Buland (EHB) bulletins prior to 2004 and the National Earthquake Information Center (NEIC) bulletins for recent events with magnitude greater than 5.5 recorded by the seismic stations in eastern Eurasia. We used event-station paths with epicentral distances between 30° and 85°. Delay times were measured by an automated waveform cross-correlation routine based on VanDecar and Crosson (1990) in three frequency bands for P waves (0.5-2.0 Hz, 0.1-0.5 Hz and 0.03-0.1Hz) and S waves (0.1-0.2 Hz, 0.05-0.1 Hz and 0.02-0.05 Hz). The signal-to-noise-ratio threshold was 20 for quality control in each frequency band and the selected records were visually inspected for consistency. The signal-to-noise ratio is defined as the ratio of the peak-to-peak amplitude of the main arrival to the standard deviation of the time series in an 80-s window before the main arrival.

To reduce the tradeoff between crustal and mantle velocity heterogeneities in seismic tomography, we removed the frequency-dependent crustal correction from the teleseismic travel times by cross-correlating the impulse responses of a crust model filtered in a narrow frequency band (Yang and Shen, 2006; Appendix I). We used a crustal model from Sun et al. (2005) for seismic stations in China, and CRUST2.0 (Bassin et al., 2000) for stations elsewhere to calculate the traveltime difference with respect to IASP91.

3.1.2. P- and S-Velocity Models in Southeast Tibet

The distribution of seismic stations in eastern Eurasia is uneven (Figure 1). In places where stations are dense, it is possible to carry out detailed data analyses to obtain high-resolution P- and S-velocity models. In addition to collecting data needed for the continental-scale inversion, these detailed studies allow us to establish references to which large-scale models can be compared. With several PASSCAL experiments (Figure 1), southeastern Tibet is such a region for a detailed study. High-resolution images of the crustal and mantle structure in the region also provide important constraints on the continental collision and plateau building processes.

We processed data from the Namche Barwa Seismic Experiment (Sol et al., 2007), which deployed a 50-station broadband array and a 20-element short-period array in southeastern Tibet during 2003-2004. Data from the GSN station LSA were also included in this study. Following the data processing method outlined above, we obtained 44,000 P and 19,500 S delay times, which were then utilized to invert for spatial variations in P- and S-wave velocity perturbations according to the 3-D finite frequency kernel formulation (Dahlen et al., 2000; Hung et al., 2004; Yang et al., 2006).

The model space is parameterized with a regular 3D grid of 33×33×33 centered at (93° E, 30° N), and has a dimension of 18° in longitude, 14° in latitude, and 1200 km in depth. The grid spacing is approximately 53 km in longitude, 46 km in latitude, and 40 km vertically. The inverse problem is resolved using a standard damped-least-square algorithm (Paige and Saunders, 1982) and the damping parameter is determined through a trade-off analysis of model norm versus variance reduction. We use checkerboard resolution tests with the same damping parameter as in the real data inversion to evaluate the ability of a given data coverage and inversion technique to recover crustal and mantle structures. These tests show that structures are well recovered beneath the stations at depth between ~50 km and ~450 km. The minimal size of the laterally and vertically resolved structure is ~100 km.

Our results (Ren and Shen, 2008; Appendix II) show a prominent N-S trending low-velocity anomaly at ~92°E down to at least 300 km depth (Figure 2). These structures are observed on both V_p and V_s models. We associate the high-velocity anomalies southwest and east of the north-south trending low velocity anomaly to the Indian lithosphere, which extends to ~250 km depth. We observe no evidence for a subducted Indian lithosphere at depth of 300 km or more beneath the study area. The north-south low velocity anomaly across Indus-Yarlung Suture coincides strikingly well with a rift on the surface at southeastern Tibet (e.g., Tappnnier and Monlar, 1977; Armijo et al., 1986; Yin, 2000) and is above a high-angle, southeastward dipping, high-velocity anomaly that extends into the upper mantle transition zone, as shown on the cross-sections (Figure 2c). We associate the high-angle dipping, high-velocity anomaly to a sunken, delaminated mantle lithosphere and the north-south-trending low-velocity structure asthenospheric upwelling induced by the sunken mantle lithosphere. The upwelling asthenospheric mantle may be responsible for the thermal weakening of the overlying crust and the localization the rifts observed on the surface of the Tibetan Plateau. Our velocity models suggest that the north-south trending rifts on the Tibetan plateau are lithosphere-scale features and the east-west extension of the plateau is mechanically coupled throughout the crust and mantle lithosphere. The relation between north-south-trending rifts on the plateau and underlying low-velocity anomalies is confirmed elsewhere in southern Tibet (Liang et al., 2008).

3.1.3. P-velocity model of East Eurasia

We also carried out inversions for the P velocity structure beneath eastern Eurasia. The tomographic model extends to 2500 km depth and is parameterized by a 81x81x51 grid with spacing of 1.0°, 1.25°, and 58 km in latitude, longitude and depth, respectively. As in the detailed study in southeast Tibet (Ren and Shen, 2008), this inversion is carried out using the finite-frequency tomography methodology (Hung et al., 2004; Yang et al. 2006). We also utilize a convolutional quelling technique (Meyerholtz et al., 1989) in this continental-scale study.

Figure 3 shows the P-velocity anomalies at 180, 270, and 540 km depth beneath east Eurasia. The model in southeast Tibet is generally consistent and comparable to the images from the detailed study (e.g., the north-south-trending low velocity anomaly).

An inspection of the sampling of the structure beneath eastern Eurasia by the finite-frequency sensitivity kernels reveals that there is a good data coverage in the depth range of 350 - 1200 km in most parts of the study area, but gaps exist in the shallow upper mantle and crust, except in regions with dense stations (e.g., southeast Tibet, Japan). Models based on teleseismic P waves have limited vertical resolution in the crust and uppermost mantle, because of steep incidence angles and lack of crossing rays at shallow depths. The problem is particularly severe in places of sparse station. To obtain a good resolution at shallow depth, we need to incorporate surface waves and regional body waves. In the crust and uppermost mantle, however, the velocity structure is highly heterogeneous and the 1D reference model used in the calculation of the "banana-doughnut" sensitivity kernels may become invalid. It is thus necessary to go beyond the 1D reference model and single-scattering approximation (Dahlen et al., 2000) and to develop a full-wave approach that accounts for complex wave interaction in the crust and shallow mantle. The following sections report the development of the finite-difference scattering-integral method (FDSIM) and its application to image the earth structure beneath eastern Eurasia.

3.2. Finite-Frequency Sensitivity Kernels for Pn/Sn Waves

We examined the finite-frequency effects and sensitivity kernels of head waves (Zhang et al., 2007), which are extremely important in determining the structure of the predominantly layered Earth. A numerical experiment was designed to demonstrate the finite-frequency effects. The model has a low-velocity layer over a high-velocity half space and a cylindrical-shaped velocity anomaly placed beneath the interface at different locations. A 3D finite-difference method (Olsen, 1994) is used to calculate synthetic waveforms. Travel-time and amplitude anomalies are measured by the cross-correlation of synthetic seismograms with and without the velocity perturbation and are compared to the 3D sensitivity kernels constructed from full waveform simulations. The results show that the head wave arrival-time and amplitude are influenced by the velocity structure surrounding the ray path in a pattern that is consistent with the Fresnel zones. Unlike the "banana-doughnut" travel-time sensitivity kernels of turning waves, the travel-time sensitivity of the head wave along the ray path below the interface is weak, but non-zero (Figure 4). Below the ray path, the travel-time sensitivity decreases with depth from the interface to a minimum (zero) before increasing to a maximum (absolute value), the depth of which depends on the wavelength and propagation distance. Thus head waves with horizontally crossing ray paths do not necessarily sample the same structure beneath the interface. The sensitivity kernels vary with the vertical velocity gradient in the lower layer, but the variation is relatively small at short propagation distances when the vertical velocity gradient is within the range of the commonly accepted values. Finally, the depression or shoaling of the interface results in increased or decreased sensitivities, respectively, beneath the interface topography (Figure 5).

3.3. Component-Dependent Sensitivity Kernels and Utility of Three-Component Seismic Records

With the exception of shear-wave splitting and receiver function analyses, the phase or amplitude anomaly of a particular arrival is usually measured on only one of the three-component seismic records. Perfectly good waveforms on the other components are often unutilized. Using full waves simulated with a finite-difference method, we demonstrate that the different components of the same arrival at the same receiver have different traveltime and amplitude sensitivities to variations in the velocity structure (Figure 6, Shen et al., 2008b). This is a finite-frequency phenomenon for measurements derived from waveforms. It is important where the scales of velocity heterogeneities are comparable or smaller than the width of the Fresnel zone. We calculate the Fréchet sensitivity kernels using the scattering-integral method (Zhao et al., 2005; Zhang et al., 2007) in conjunction with finite-difference wave simulation in three-dimensional media. The differences in the sensitivity kernels for the different components vary with the wave type, source-receiver geometry, and source mechanism (Shen et al., 2008b). They are attributed to scattered waves that affect the waveforms on the different components by various amounts. Thus the differential kernels between the different components of the same arrival may enable us to use the corresponding phase and amplitude measurements, which are relatively accurate observations unaffected by uncertainties in source origin time and location, to image the earth structure, particularly fine structures near receivers.

3.4. Finite-Frequency Ambient Noise Tomography

Previous studies have demonstrated the efficacy of extracting information on crustal and shallow mantle structure from seismic noise (e.g., Shapiro and Campillo, 2004; Sabra et al., 2005; Shapiro et al., 2005; Yao et al., 2006; Yang et al., 2007; Cho et al., 2007; Lin et al., 2008). The fact that the estimated Green's function is based on cross-correlation of ambient noise makes it straightforward to adapt this type of measurements to the frequency-dependent phase-delay anomalies.

We have collected and processed continuous data from 50 broadband stations deployed in the Namche Barwa seismic experiment in southeast Tibet during 2003-2004 (Sol et al., 2007). We use all three components and computed the cross-correlations between all possible pairs of components from pairs of stations in order to obtain the estimated Green's functions. The raw data are cut into one-day-length waveforms. The mean, trend and instrument response are removed and the data are bandpass filtered between 4 s and 150 s period, and one-bit normalized. The data are then cross-correlated and stacked. The observed signals at positive and negative and positive correlation lag times correspond to waves propagating in opposite directions between two stations. We measure the phase delays between the estimated Green's function and the synthetics calculated using a non-staggered finite difference method (Zhang and Chen, 2006), which takes into account not only 3D velocity heterogeneities but also topography variations. For the reference model, we use a modified crustal model, CRUST 2.0 to approximate the 3D wave-speed variations in the crust, and the ak135 for the mantle part. We replace the top two sediment layers in CRUST 2.0 with a global sediment layer model digitized at 1°x1° cells. Topography is incorporated in the finite-difference model.

Unlike previous studies that use the estimated Green's functions to solve for phase or group velocity maps and then a point-wise S velocity structure under a 1D assumption (e.g., Yao et al., 2006; Yang et al., 2007; Cho et al., 2007), we construct 3D sensitivity kernels for the finite-frequency Green's functions (Ren et al., 2008). The kernels are calculated using the finite-difference scattering-integral method (Zhao et al., 2005; Zhang et al., 2007; Zhang and Shen, 2008). Depending on the wave period and scales of topography, both the shallow velocity structure and surface topography may significantly affect the 3D sensitivity kernels (Zhang and Shen, 2007). Figure 7 shows an example of the sensitivity kernels between two stations in southeast Tibet. The sensitivity kernels and the phase delays between the estimated Green's functions and synthetics are inverted for Vp and Vs structure beneath southeast Tibet. Figure 8 shows the Vs velocity perturbations relative to 3D reference model. The broad low Vs anomaly in the lower crust suggests that the wave speed in the reference model is too high in the lower crust. On the other hand, the high Vs anomaly in the shallow crust suggests that the wave speed in the reference model is too low in the shallow crust.

4. DISCUSSION AND CONCLUSIONS

In the past few years, the finite-frequency theory has experienced a rapid development from the "banana-doughnut" sensitivity kernels based on a 1D reference model and single- and forward-scattering to a full-wave approach based on a finite-difference or spectral-element method. Though approximate, the 1D-reference approach is relatively computationally efficient, making it well suited for high-frequency teleseismic body wave tomography. The application of this method with finite-frequency teleseismic body wave traveltimes has led to new observations of plume-like features in the lower mantle (Montelli et al., 2004). It has also been adapted in various regional crustal and mantle teleseismic tomography (Hung et al., 2004; Yang et al., 2006; Ren and Shen, 2008; Liang et al., 2008; Allen et al., 2008; Wolfe et al., 2008). Our results show that the method works well in places with dense stations such as southeast Tibet (Figure 2). Although the broad sensitivity kernels of low-frequency body waves help to alleviate the problem of uneven sampling of the mantle structure beneath east Eurasia, they do not compensate for sparse station coverage and a near vertical incidence of teleseismic body waves at shallow depth (Figure 3).

To date, two methods have been developed to carry out full-wave tomography iteratively with 3D reference models. One is the adjoint-wavefield (AW) method, which back-propagates the data from the receivers to image structure (Tromp et al., 2005; Liu and Tromp, 2006). The other is the scattering-integral (SI) method, which calculates and stores the sensitivity kernels for each data functional (Zhao et al., 2005; Zhang et al., 2007). The AW approach has been integrated with a spectral-element method (Komatitsch et al., 2005) for wave-propagation simulation and the SI approach a finite-difference method (Olsen, 1994; Zhang and Chen, 2006). Each approach has its advantages and disadvantages. A notable advantage of the SI method is that it provides both the Hessian and gradient of the misfit function in the tomographic inversion and requires a fewer number of simulations per model iteration to achieve the same level of data variance reduction (Chen et al., 2007a). The disadvantage is that it requires a much larger disk storage than the AW method. Depending on the available computational resources and the numbers of sources and receivers, one approach may be more computationally efficient than the other.

We have focused our efforts on the development and application of the finite-difference, scattering-integral method (FDSIM). We have numerically validated the scattering-integral sensitivity kernels for 3D reference models (Zhang et al., 2007). We show that the head wave arrival-time and amplitude are influenced by the velocity structure surrounding the ray path in a pattern that is consistent with the Fresnel zones. The travel-time sensitivity of the head wave is week along the ray path below the interface, but non-zero. Below the ray path, the travel-time sensitivity decreases with depth from the interface to a minimum (zero) before increasing to a maximum (absolute value), the depth of which depends on the wavelength and propagation distance. We demonstrate that the different components of the same arrival have different traveltime and amplitude sensitivities to the 3D velocity structure due uneven distribution of scattered waves on the different components of the same arrival (Shen et al., 2008b). Furthermore we apply the FDSIM methodology to surface-wave tomography using ambient seismic noise. Unlike previous studies that use estimated Green's functions to solve for phase or group velocity maps and then a point-wise S velocity structure under a 1D assumption, we construct 3D sensitivity kernels for the finite-frequency Green's functions, taking into account a 3D reference model and the effects of topographic variations. The sensitivity kernels and the phase delays between the estimated Green's functions and synthetics are inverted for Vp and Vs structure beneath southeast Tibet (Ren et al., 2008). Results show that the wave speed in the reference model (a modified CRUST 2.0) is too high in the lower crust and too low in the shallow crust beneath southeast Tibet.

5. RECOMMENDATIONS

The full-wave approach accounts for complex wave propagation in 3D reference models, enables fuller utilization of an arrival on all three components of seismic records, and allows us to linearize the inverse problem by iteratively updating the 3D reference model. An important benefit of physically realistic and accurate modeling of full wavefields in 3D models is the consistency of the system of equations in inversion. This is particularly important for the integration of different types of observations (P, S, and surface waves) and physical properties (wave speed or elastic parameters, attenuation, and anisotropy) in inversion, which is a challenging but essential step to obtain a coherent and self-consistent image of the crust and mantle. One notable benefit of the full-wave approach is that the new method makes it unnecessary to identify and separate body and surface waves. It thus provides a natural way to integrate the constraints from various wave types. With the ever-increasing high-performance computational power, this full-wave approach will become a more and more practical and powerful tool. Peta-scale computing systems (e.g., Blue Waters, a NSF-sponsored system), for instance, will be available for scientific applications in the next few years. We anticipate that such facilities will take the full-wave approach to a new level.

The applications of our FDSIM are limited by computational resources. The greater the computational resources we have, the larger the geographic area we can study or the higher frequency waves we can use. Nevertheless, to utilize high-frequency (0.2 – 1 Hz) teleseismic body waves in regional tomography, it will be necessary in the near future to develop a coupled 1D-3D approach, in which waves outside of the volume of interest propagate within a 1D model and those inside the volume of interest are treated with a full 3D numerical method.

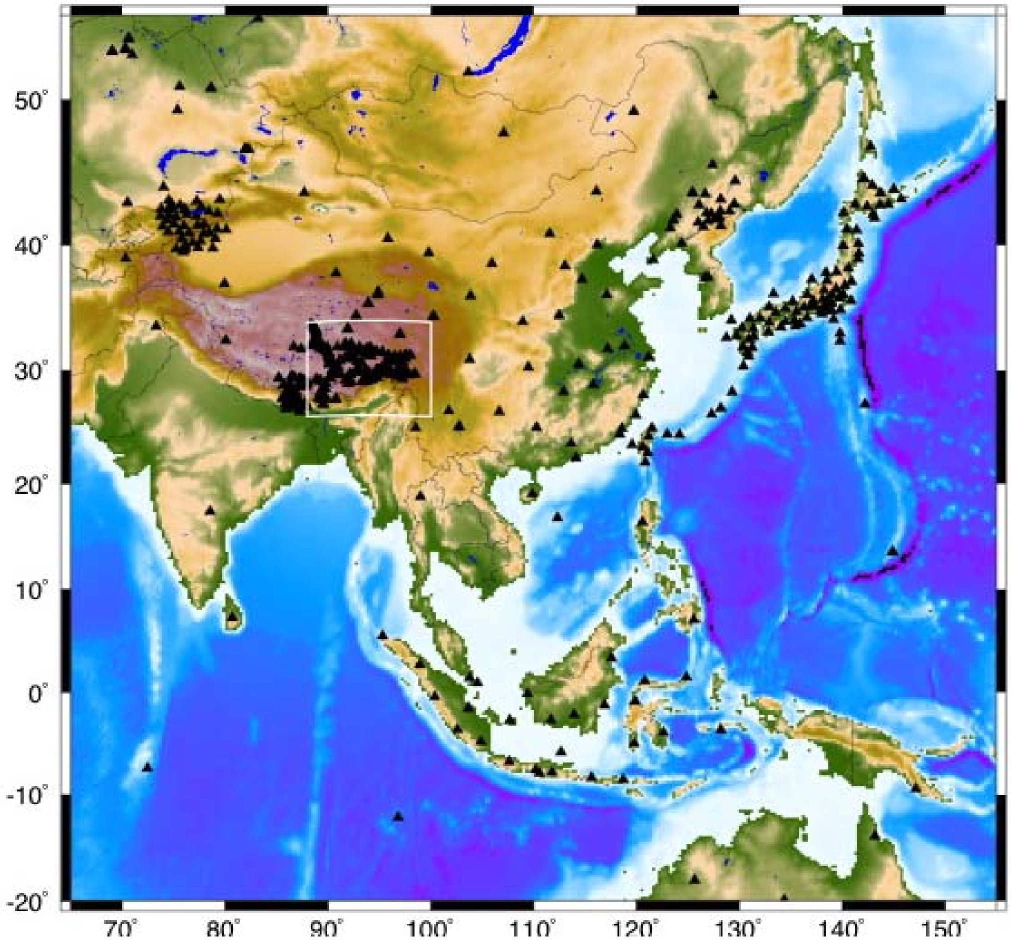
50°
40°
30°
20°
10°
0°
-10°
-20°
70°
80°
90°
100°
110°
120°
130°
140°
150°

Figure 1 Topography of Eastern Eurasia and the distribution of broadband seismic stations used in this study (triangles). The box outlines a detailed finite-frequency teleseismic traveltime tomographic study in southeastern Tibet.

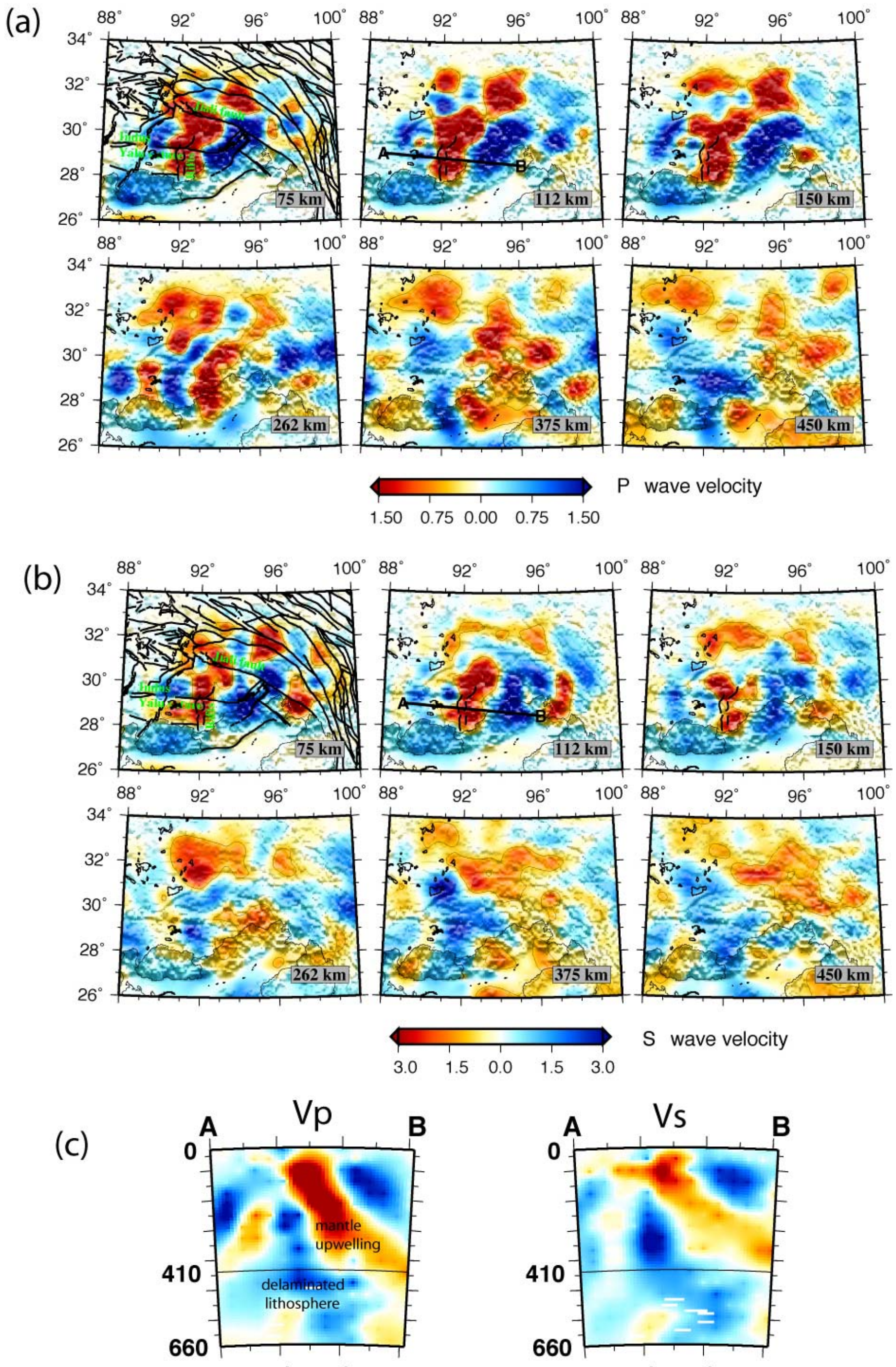
(a)
88°
92°
96°
100°
34°
32°
30°
28°
26°
Jiali fault
Indus
Yalu suture
Rifts
75 km
A
B
112 km
150 km
262 km
375 km
450 km
P wave velocity
1.50
0.75
0.00
0.75
1.50
(b)
75 km
112 km
150 km
262 km
375 km
450 km
S wave velocity
3.0
1.5
0.0
1.5
3.0
(c)
Vp
Vs
A
B
0
410
660
mantle upwelling
delaminated lithosphere
0°
2°
4°
6°

Figure 2 (a) P-velocity perturbations at several depths beneath southeastern Tibet: 75 km, 112 km, 150 km, 262 km, 375 km, and 450 km. Black lines in the 75-km horizontal slice represent the known faults. Notice the north-south trending rift coincides with a prominent north-south trending low-velocity anomaly. Line AB on the 112-km-depth image marks the location of the vertical profile in (c). (b) S-velocity perturbations at the same depths. (c) Cross-section A-B through P and S-wave tomographic models, along the Indus-Yarlung suture and across a rift in southeastern Tibet. From Ren and Shen (2008).

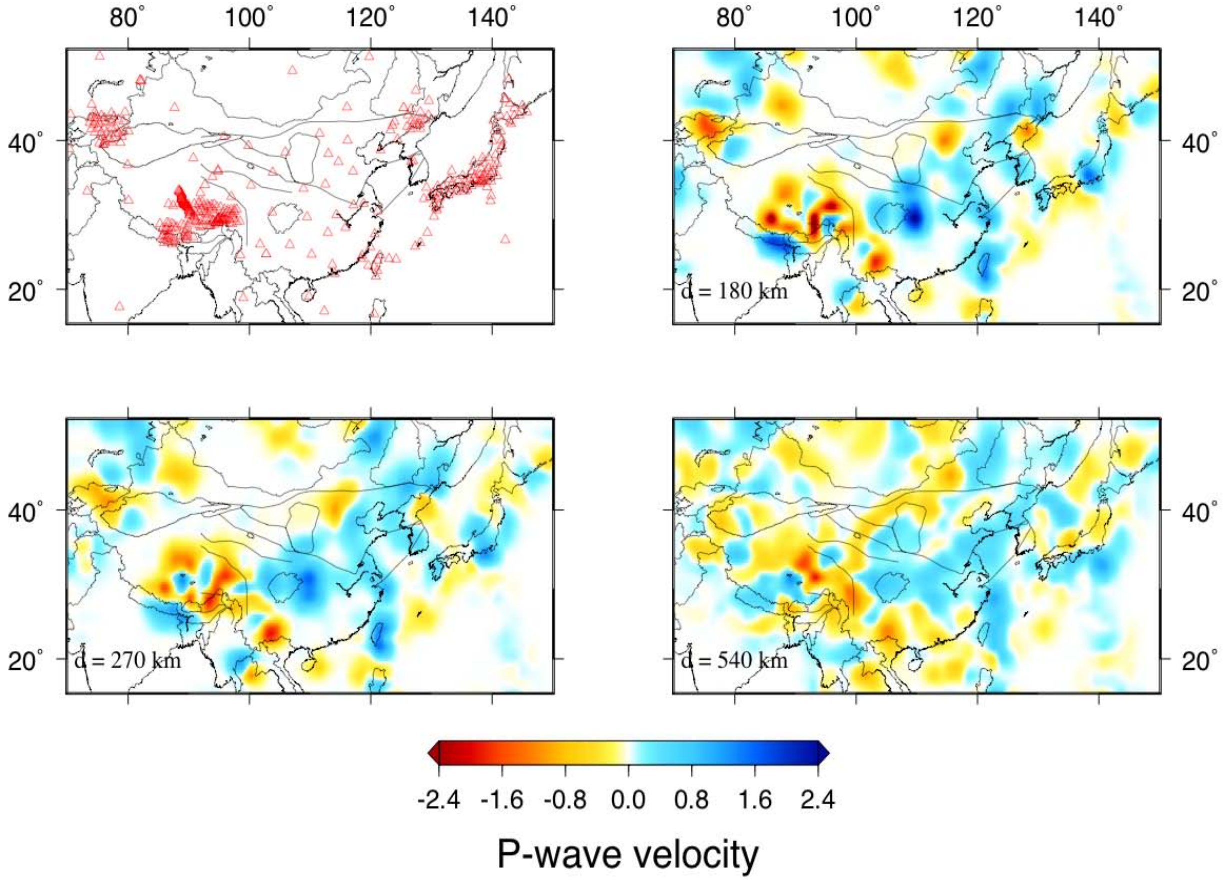
80°
100°
120°
140°
40°
20°
d = 180 km
d = 270 km
d = 540 km
-2.4
-1.6
-0.8
0.0
0.8
1.6
2.4
P-wave velocity

Figure 3 The P-velocity variations relative to iasp91 at 180, 270 and 540 km depth. Triangles in the upper left panel show the distribution of the broadband stations used in eastern Eurasia.

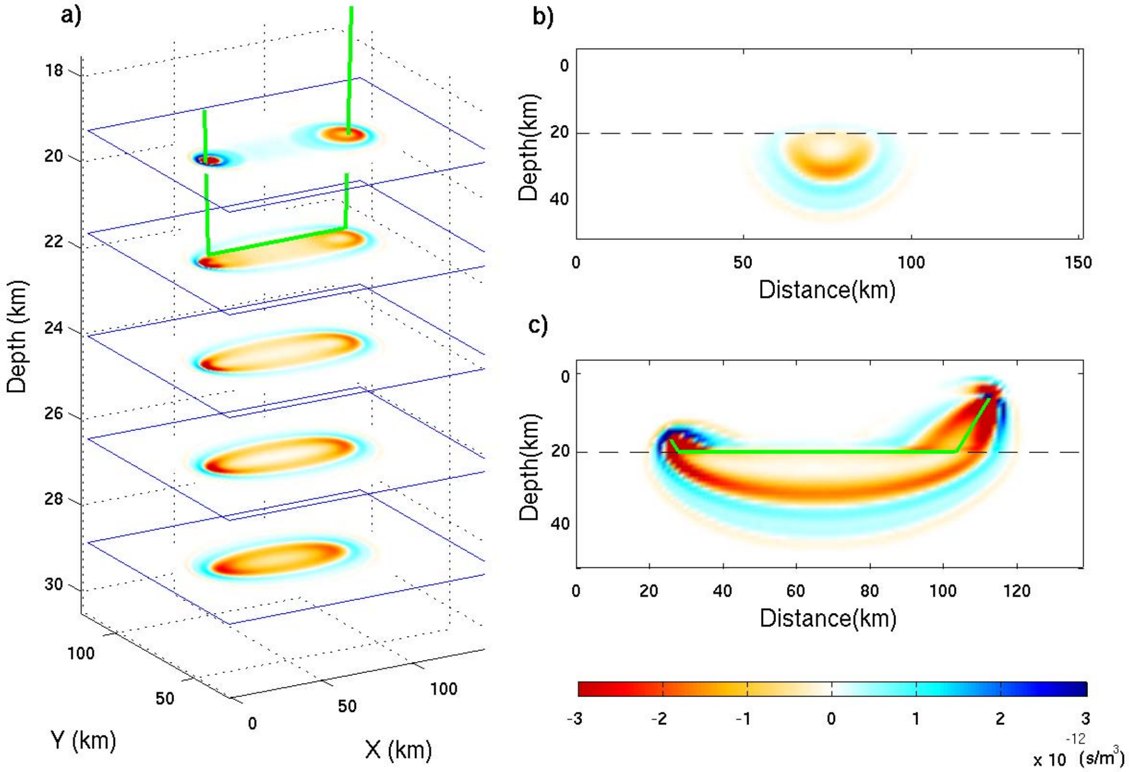

Figure 4 (a) The traveltime sensitivity kernels for the head wave recorded on the vertical component on the horizontal planes at depths below (21.6 km, 24 km, 26.4 km, 28.8 km) and above (19.2 km) the interface that separates the low and high velocity layers. The green line marks the head wave ray path. The source is located on the left side of this figure. The negative (red colors) and positive (blue colors) values are so defined that a low-velocity anomaly located in the region of the negative kernels results in a travel time delay and the same velocity perturbation in the region of positive kernels leads to an earlier head wave arrival. (b) The traveltime sensitivity kernel for the head wave on a vertical profile half way between the source and receiver and perpendicular to the ray path. The dashed line is the layer interface. (c) The traveltime sensitivity kernels for the head wave on the vertical profile containing the source and receiver. The full range of the kernels is -4.83-1.655×10^{-11} s/m^3. From Zhang et al. (2007).

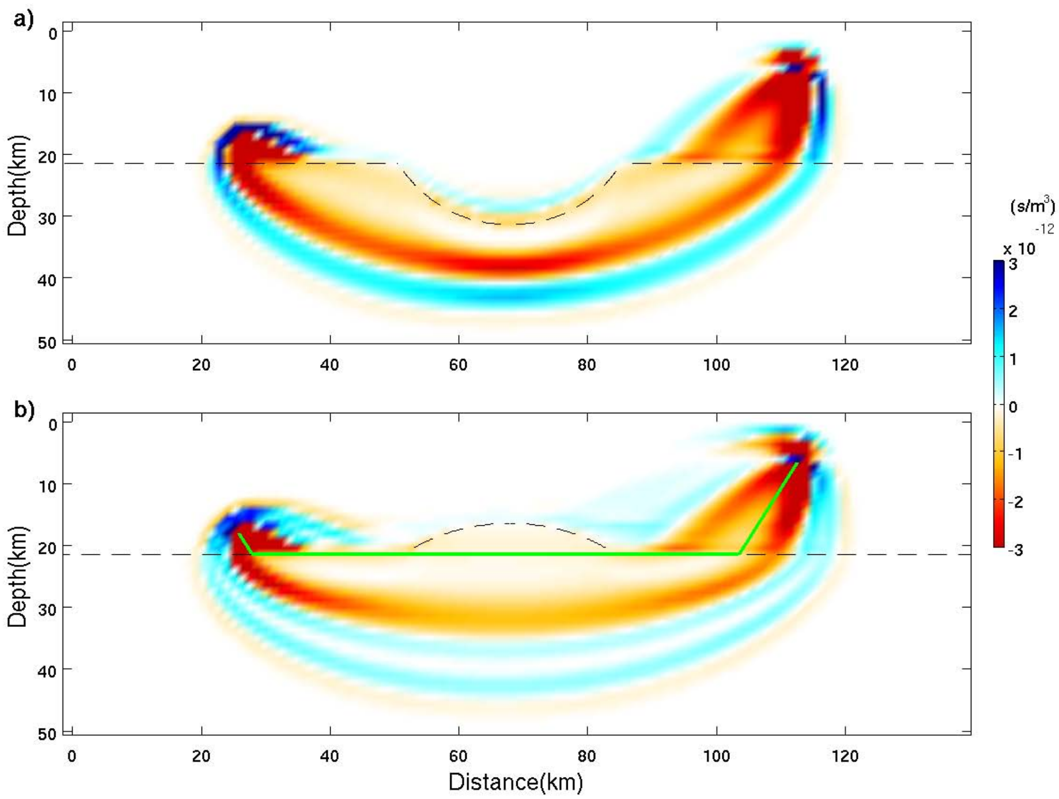

Figure 5 The kernels for the vertical component of head waves in the models with up-bending and down-bending layer interface between the source and receiver. Except for the perturbed interface, all other parameters of the models are the same as those of the model in Fig. 4. Note that the interface variation is cylindrical with the symmetric axis perpendicular to the plane containing the source-receiver path, not spherical. The dashed line indicates the layer interface and the green line highlights the head wave ray path. The meanings of the positive and negative values are the same as those in Fig. 4. (a) A cylindrical down-bending interface with the maximum depression of 10 km and a horizontal dimension of 35 km. The full range of the kernel is -5.19-1.75×10^{-11}s/m^3 (b) An up-bending interface. The maximum shoaling is 5 km, and the horizontal dimension of the interface perturbation is 35 km. The full range of the kernel is -3.82-1.43×10^{-11}s/m^3. From Zhang et al., (2007).

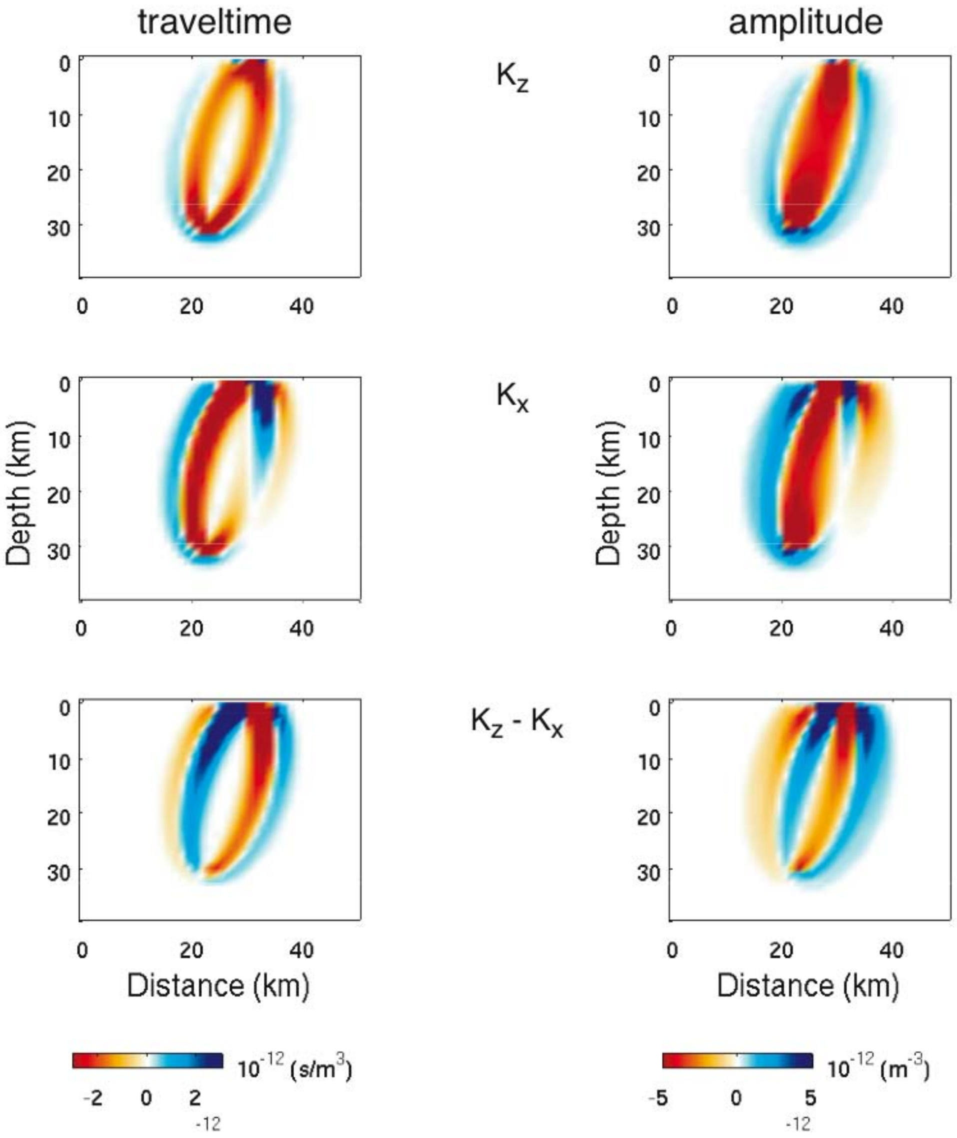

Figure 6 Delay-time (left) and amplitude (right) sensitivity kernels for the z and x components and their differential kernel. The surface receiver (30.8 km, 0) is at a relatively short horizontal distance from the explosive source at depth (22.8 km, 30.0 km). The negative (red colors) and positive (blue colors) values for traveltimes are so defined that a low-velocity anomaly located in the region of the negative kernels results in a phase delay and the same velocity perturbation in the region of positive kernels leads to an earlier arrival as measured by waveform cross-correlation. For amplitude, the negative (red colors) and positive (blue colors) values are so defined that a high-velocity anomaly located in the region of the negative kernels results in an amplitude reduction and the same velocity perturbation in the region of positive kernels leads to an increase in amplitude. From Shen et al. (2008).

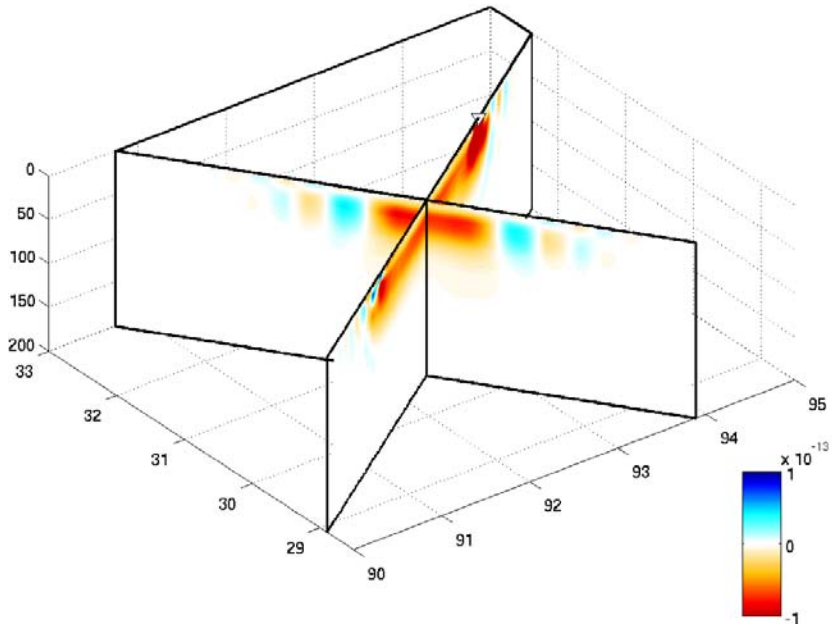

Figure 7 Cross-sections of phase-delay sensitivities (in s/m^3) to Vs perturbations between the vertical components of two seismic stations in southeast Tibet for wave periods of 20-30 s. The phase-delays are sensitive also to Vp perturbations at shallow depths (not shown).

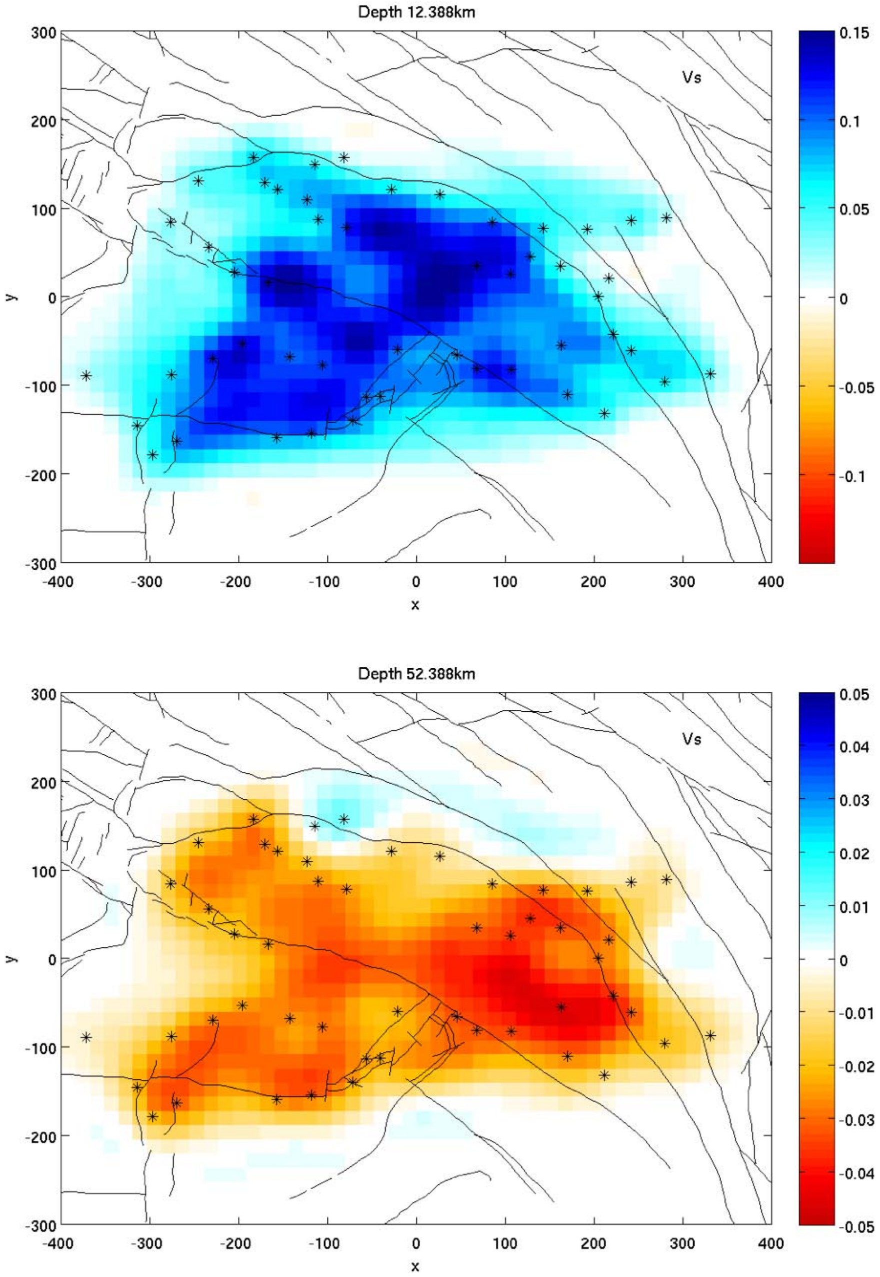
Depth 12.388km
Vs
300
200
100
0
-100
-200
-300
y
-400
-300
-200
-100
0
100
200
300
400
x
0.15
0.1
0.05
0
-0.05
-0.1
Depth 52.388km
Vs
300
200
100
0
-100
-200
-300
y
-400
-300
-200
-100
0
100
200
300
400
x
0.05
0.04
0.03
0.02
0.01
0
-0.01
-0.02
-0.03
-0.04
-0.05

Figure 8 Preliminary Vs perturbation models from the inversion of estimated Green's function phase delays at 12 km (upper panel) and 52 km depth (lower panel). The anomaly is relative to the 3D reference model, a modified CRUST 2.0. The color scale is ±15% (top panel) and ±5% (lower panel), respectively.

REFERENCES

Allen, R., X. Mei, S.-H. Hung, Using Finite-frequency methods to improve regional models, Eos Trans. AGU, 89(53), Fall Meet. Suppl., Abstract S21D-02, 2008.

Armijo, R., P. Tapponnier, J.P. Mercier, and T. Han, Quaternary extension in southern Tibet, J. Geophys. Res., 91, 13,803-13,872,1986.

Baig, A.M., F.A. Dahlen, and S.-H. Hung, Traveltimes of waves in three-dimensional random media, Geophys. J. Int., 153, 467-482, 2003.

Bassin, C., G. Laske, and G. Masters, The current limits of resolution for surface wave tomography in North America, EOS, Trans. Am. Geophys. Un. 81, F897, 2000.

Chen, P., T.H. Jordan, and L. Zhao, Full three-dimensional tomography: a comparison between the scattering-integral and adjoint-wavefield methods, Geophys. J. Int., 170, 175-181, 2007a.

Chen, P., L. Zhao, and T.H. Jordan, Full 3D tomography for crustal structure of the Los Angeles Region, Bull. Seismol. Soc. Am., 97 (4), 1094-1120, doi: 10.1785/0120060222, 2007b.

Cho, K.H., R.B. Herrmann, C.J. Ammon, K. Lee, Imaging the upper crust of the Korea Peninsula by surface-wave tomography, Bull. Seismol. Soc. Am., 97 (1B), 198-207, doi: 10.1785/0120060096, 2007.

Dahlen, F.A., Hung, S.-H., & Nolet, G., Fréchet kernels for finite frequency traveltimes-I. Theory, Geophys. J. Int., 141, 157-174, 2000.

Hung, S.-H., F.A. Dahlen, and G. Nolet, Fréchet kernels for finite-frequency traveltimes-II. Examples, Geophys. J. Int., 141, 175-203, 2000.

Hung, S-H ,Y. Shen, and L.-Y. Chiao, Imaging seismic velocity structure beneath the Iceland hot spot: A finite frequency approach, J. Geophy. Res., 109, doi: 10.1029/2003JB002889, 2004.

Komatitsch, D., S. Tsuboi, and J. Tromp, The spectral-element method in seismology in Seismic Earth: Array Analysis of Broadband Seismograms, Geophysical Monograph Series 157, AGU, 10.1029/156GM13, 2005.

Li, X., and B. Romanowicz, Global mantle shear velocity model developed using nonlinear asymptotic coupling theory, J. Geophys. Res., 101, 22,245-22,272, 1996.

Liang, X., Y. Shen, Y.J. Chen, and Y. Ren, Crustal and mantle velocity models of southern Tibet from finite-frequency tomography, Eos Trans. AGU, 89(53), Fall Meet. Suppl., Abstract T13B-1955, 2008.

Lin, F., M.P. Moschetti, and M.H. Ritzwoller, Surface wave tomography of the western United States from ambient seismic noise: Rayleigh and Love wave phase velocity maps, Geophys. J. Int., doi:10.1111/j1365-246X.2008.03720.x, 2008.

Liu, Q., and J. Tromp, Finite-frequency kernels based on adjoint methods, Bull. Seismol. Soc. Am. 96, 2383-2397, 2006.

Meyerholtz, K. A., G. L. Pavlis, and S. A Szpakowski, Convolutional quelling in seismic tomography, Geophysics, 54, 570-580, 1989.

Montelli R., G. Nolet, G. Masters, F.A. Dahlen, and S.-H. Hung, Global P and PP traveltime tomography: rays versus waves, Geophys. J. Int., 158, 637-654, 2004.

Montelli, R., G. Nolet, F.A. Dahlen and G. Masters, A catalogue of deep mantle plumes: new results from finite-frequency tomography, Geochem. Geophys. Geosyst. (G3), **7** , Q11007, doi:10.1029/2006GC001248, 2006.

Nolet, G., and F.A. Dahlen, Wave front healing and the evolution of seismic delay times, J. Geophys. Res., 105 (B5), 19,043-19,054, 2000.

Olsen, K.B., Simulation of three-dimensional wave propagation in the Salt Lake Basin, Ph.D. Thesis, University of Utah, Salt Lake City, Utah, 157p, 1994.

Paige, C.C., and M. A. Saunders, LSQR: An algorithm for sparse linear-equations and sparse least-squares, Trans. Math. Software, 8, 43-71, 1982.

Ren, Y., Y. Shen, Finite-frequency tomography in southeastern Tibet: Evidence for the causal relation between mantle lithosphere delamination and the north-south-trending rifts, J. Geophys. Res., 113, B10316, doi:10.1029/2008JB005615, 2008.

Ren, Y., W. Zhang, Y. Shen, Crustal and uppermost mantle structures beneath the southeastern Tibet from 3D full- wavefield finite-frequency tomography using ambient seismic noise, Eos Trans. AGU, 89(53), Fall Meet. Suppl., abstract T13B-1954, 2008.

Ritzwoller, M.H., NM. Shapiro, M.P. Barmin, and A.L. Levshin, Global surface wave diffraction tomography, J. Geophys. Res., 107, DOI: 10.1029/2002JB001777, 2002.

Sabra, K.G., P. Gerstoft, P. Roux, W.A. Kuperman, Extracting time-domain Green's function estimates from ambient seismic noise, Geophys. Res. Lett., 32, L03310, doi: 10.1029/2004GL021862, 2005.

Shapiro, N.M. and M. Campillo, Emergence of broadband Rayleigh waves from correlations of the ambient seismic noise, Geophys. Res. Lett., 31, L07614, doi: 10.1029/2004GLL019491, 2004.

Shapiro, N.M., M. Campillo, L. Stehly, and M.H. Ritzwoller, High-resolution surface-wave tomography from ambient seismic noise, Science, 207, 1615-1618, 2005.

Shen, Y., W. Zhang, Y. Ren, and X. Liang, Imaging the crust and upper mantle in the southern and southeastern Tibetan plateau: A three-dimensional full-wavefield approach, Eos Trans. AGU, 89(53), Fall Meet. Suppl., abstract T11E-06, 2008a.

Shen, Y., Z. Zhang, L. Zhao, Component-dependent Frechet sensitivity kernels and utility of three-component seismic records, Bull. Seismol. Soc. Am., 98 (5), 2517-2525, doi: 10.1785/0120070283, 2008b.

Sigloch, K., N. McQuarrie, G. Nolet, Two-stage subduction history under North America inferred from multiple-frequency tomography, Nature Geosci., 1, 458-462, 2008.

Sol, S., A. Meltzer, R. Burgmann, R.D. van der Hilst, R. King, Z. Chen, P.O. Koons, E. Lev, Y.P. Liu, P.K. Zeitler, X. Zhang, J. Zhang, and B. Zurek, Geodynamics of the southeastern Tibetan Plateau from seismic anisotropy and geodesy, Geology, 35, 563-566, doi:10.1130/G23408A.1, 2007.

Sun, Y., L. Xu, S. Kuleli, F. D. Morgan, and M. N. Toksoz, Adaptive moving window method for 3-D P-velocity tomography and its application in China. Bull. Seismol. Soc. Am., 94, 2, 740-746, 2004.

Tromp, J., C.H. Tape, and Q. Liu, Seismic tomography, adjoint methods, time reversal, and banana-doughnut kernels. Geophys. J. Int., 160, 195-216, 2005.

VanDecar, J. C., and R. S. Crosson, Determination of teleseismic relative phase arrival times using multi-channel cross-correlation and least squares, Bull. Seismol. Soc. Am., 80, 150-169, 1990.

Wolfe C., S. Solomon, G. Laske, J. Collins, R. Detrick, J. Orcutt, D. Bercovici, and E. Hauri, S-wave tomographic imaging of the mantle beneath the Hawaiian Islands from the PLUME deployments of ocean-bottom and land seismometers, Eos Trans. AGU, 89(53), Fall Meet. Suppl., Abstract DI21A-1725, 2008.

Yang, T. and Y. Shen, Frequency dependent crustal correction for finite frequency seismic tomography, Bull. Seismol. Soc. Am., 96 (6), 2441-2448, doi:10.1785/0120060038, 2006.

Yang, T., Y. Shen, S. van der Lee, S.C. Solomon, S.-H. Hung, Upper mantle structure beneath the Azores hotspot from finite-frequency seismic tomography, Earth Planet. Sci. Lett., 250, 11-26, 2006.

Yang, Y., M.H. Ritzwoller, A.L. Levshi, and N.M. Shapiro, Ambient noise Rayleigh wave tomography across Europe, Geophys. J. Int., 168, 259-274, 2007.

Yao, H., R.D. van der Hilst, M.V. de Hoop, Surface-wave array tomography in SE Tibet from ambient seismic noise and two-station analysis –I. Phase velocity maps, Geophys. J. Int., 166, 732-744, doi: 10.1111/j.1365-246X.2006.03028.x, 2006.

Yin, A., Mode of Cenozoic east-west extension in Tibet suggesting a common origin of rifts in Asia during the Indo-Asian collision, J. Geophys. Res., 105, 21,745-21,759, 2000.

Yoshizawa, K., and B.L.N. Kennett, Determination of the influence zone for surface wave paths, Geophys. J. Int. 149, 440-453, 2002.

Zhang, W., and X.F. Chen Traction image method for irregular free surface boundary in finite difference seismic wave simulation, Geophys J Int, 167(1), 337-353, 2006.

Zhang, W., and Y. Shen, Finite-Frequency Tomography Using Ambient Seismic Noise in the Presence of Surface Topography, Eos Trans. AGU, 88(52), Fall Meet. Suppl., Abstract S23B-1384, 2007.

Zhang, Z., Y. Shen, L. Zhao, Finite-frequency sensitivity kernels for head waves, Geophys. J. Int., 171, 847-856, doi:10.1111/j.1365-246X.2007.03575.x, 2007.

Zhao, L. and T.H. Jordan, Structural sensitivities of finite-frequency seismic waves: a full-wave approach, Geophys. J. Int., 165, 981-990, doi:10.1111/j.1365-246X.2006.02993.x, 2006.

Zhao, L., T.H. Jordan, and C.H. Chapman, Three-dimensional Fréchet differential kernels for seismic delay times, Geophys. J. Int., 141, 558-576, 2000.

Zhao, L., T.H. Jordan, K.B. Olsen, and P. Chen, Frechet kernels for imaging regional earth structure based on three-dimensional reference models, Bull. Seismol. Soc. Am., 95, 2066-2080, 2005.

Zhou, Y., F.A.Dahlen, and G. Nolet, 3-D sensitivity kernels for surface-wave observables, Geophys. J. Int, 158, 142-168, 2004.

Zhou, Y., F.A. Dahlen, G. Nolet, G. Laske, Finite-frequency effects in global surface-wave tomography, Geophys. J. Int., 153, 1087-1111, doi:10.1111/j.1365-264X.2005.02780.x, 2005.

Zhou, Y., G. Nolet, F. A. Dahlen, and G. Laske, Global upper-mantle structure from finite-frequency surface-wave tomography" Journal of Geophysical Research, 111, B04304, doi:10.1029/2005JB003677, 2006.

LIST OF SYMBOLS, ABBREVIATIONS, AND ACRONYMS

AFRL	Air Force Research Laboratory
AW	Adjoint wavefield
DMC	Data Management Center
EHB	Engdahl-van der Hilst-Buland
FDSIM	finite-difference, scattering-integral method
GSN	Global Seismographic Network
IRIS	Incorporated Research Institutions for Seismology
JISNET	Japan-Indonesia Seismic Network
NEIC	National Earthquake Information Center
PASSCAL	Program for Array Seismic Studies of the Continental Lithosphere
SI	Scattering Integral

APPENDIX I.

Frequency-Dependent Crustal Correction for Finite-Frequency Seismic Tomography

by Ting Yang and Yang Shen

Bulletin of the Seismological Society of America, Vol. 96, No. 6, pp. 2441–2448 December 2006, doi: 10.1785/0120060038

Short Note

Frequency-Dependent Crustal Correction for Finite-Frequency Seismic Tomography

by Ting Yang* and Yang Shen

Abstract Removing the crustal signature from teleseismic travel times is an important procedure to reduce the trade-off between crustal and mantle velocity heterogeneities in seismic tomography. Because reverberations of long- and short-period body-wave arrivals in the crust affect the waveforms of the direct arrivals differently, the crustal effects on travel times measured by waveform cross correlation are frequency dependent. With synthetic responses of selected crustal models, this short note illustrates the significance of frequency-dependent crustal corrections to finite-frequency body-wave travel-time tomography. The differences in crustal correction between long- and short-period body waves at the same station can be as large as 0.6 sec, depending on the crustal thickness, velocity contrast at the Moho, and layering within the crust.

Introduction

Variations in station elevation and crustal structure beneath seismic stations are responsible for a significant fraction of observed teleseismic body-wave travel-time anomalies. In regions having large variations in crustal thickness (e.g., eastern Eurasia and central Andes) or complex crustal structure, the crust may account for half of the observed travel-time residuals (Kissling, 1993; Beck *et al.*, 1996; Martin *et al.*, 2005). In teleseismic body-wave tomographic studies, the crustal and shallow-mantle structure usually cannot be directly resolved in the inversion because incident waves from teleseismic events propagate nearly vertically and do not cross each other at shallow depths (e.g., Wolfe *et al.*, 1997). If crustal anomalies are not removed from travel-time residuals, they tend to be mapped into deeper mantle, causing artificial velocity anomalies in tomographic models (e.g., Waldhauser *et al.*, 2002). Travel-time correction for shallow structure, therefore, has been an essential procedure in seismic tomography to improve the resolution in the mantle.

There are two common approaches to cope with this problem. The first is to add an additional unknown for each station to be solved in the inversion (e.g., Evans and Achauer, 1993; VanDecar *et al.*, 1995; Wolfe *et al.*, 1997; Foulger *et al.*, 2001). These additional unknowns, or station terms, are used to account for travel-time anomalies associated with the crustal and shallow-mantle structure and are solved simultaneously with the velocity structure in the inversion. One notable characteristic of this approach is that the station terms include the effects from both the crust and shallow mantle. Thus for studies with a large station spacing, the shallow-mantle structure is usually “absorbed” into the station terms and unresolved. By definition, the station terms do not vary with frequencies, epicentral distances, and backazimuths of incoming waves.

For regions where the crustal structure has been determined from other observations such as surface-wave studies, receiver function analyses, and/or reflection and refraction seismic profiles, the crustal effects relative to a reference model can be removed by subtracting the travel-time anomalies accrued within the crust from the total travel-time delays. The residual travel-time delays are then used to invert the mantle structure (e.g., Dawson *et al.*, 1990; Allen *et al.*, 2002; Keyser *et al.*, 2002). Compared with the station-term method, this approach is valuable for imaging the shallow-mantle structure (e.g., Allen *et al.*, 2002), in particular, when the *a priori* crustal structure is considered to be well constrained. Crustal corrections in this approach may vary with epicentral distances and backazimuths of incoming waves. They are usually calculated for the direct arrival under ray theory without any consideration to the reverberation of the wave in the crust (e.g., Allen *et al.*, 2002; Waldhauser *et al.*, 2002; Hung *et al.*, 2004; Martin *et al.*, 2005). When the arrival time of a seismic phase is handpicked from the onset of the arrival, ray theory is commonly used and justified by the argument that the onset represents the arrival of the highest-frequency signal in the seismogram. But it is often difficult to pick the onset of the arrival accurately when the arrivals are long period, emergent, or of less-than-excellent signal-to-noise ratio.

---

*Present address: Jackson School of Geoscience, the University of Texas at Austin, 1 University Station C1100, Austin, Texas 78712.

The availability of digital seismic records has made it a common practice to obtain travel times by cross-correlating seismic waveforms (VanDecar and Crosson, 1990). For finite-frequency seismic signals, reverberations of the arrival in the crust beneath a station may overlap with the direct arrival and thus may significantly change the waveform of the direct arrival. The travel times obtained by waveform cross-correlation are therefore sensitive to crust reverberations, especially at low frequencies and for the crust with strong reflectors at shallow depth. As a result, the correction calculated for the direct ray path under ray theory cannot fully account for the effects of crustal variations on travel times measured by waveform cross correlation.

This problem is often neglected in ray-based tomography and has now become more severe for the newly developed finite-frequency seismic tomography (FFST), in which the travel-time calculation is based on 3D sensitivity kernels (Dahlen *et al.*, 2000) instead of ray theory. Because the 3D volumes of low-frequency kernels are broader than those of higher-frequency signals, low-frequency signals offer constraints on the structure farther away from geometrical rays. This more realistic representation of wave propagation helps to obtain a smoother, more even sampling of the velocity structure beneath stations. At ocean bottom and ocean island environments, where the microseism is high (Wilcock *et al.*, 1999), most useful arrivals with good signal-to-noise ratios are in the low-noise notch (roughly 0.03–0.1 Hz; Webb, 1998), the low-frequency range in teleseismic body-wave tomography. To isolate the microseism, Hung *et al.* (2004), Shen and Hung (2004), and Yang *et al.* (2006) filtered broadband *P*-wave records in the high-, intermediate-, and low-frequency bands (0.5–2, 0.1–0.5, and 0.03–0.1 Hz, respectively), and combined the travel times measured in the three frequency ranges in joint tomographic inversions. About 60% of the useful *P*-wave arrivals in the Iceland data set, for example, is long period. For these reasons, long-period travel-time data and their correction for crustal effects are important in FFST, which offers the potential to utilize more information in broadband waveforms than ray theory.

Here we present a crustal correction method, in which crustal reverberations for arrivals with different frequencies are taken into account. Using synthetic waveforms, we show that the crustal correction can be approximated by the waveform shift measured by cross correlation of the response of a given crustal model and that of the reference model in a narrow-frequency band.

Effects of Crustal Reverberations on Travel Times

We use synthetic seismograms to demonstrate that the effects of body-wave reverberations in the crust beneath a station on travel times measured by waveform cross correlation are frequency dependent. We construct synthetic seismograms by convolving a source time series with the impulse response of a crustal model. Our source function is chosen to be the first derivative of a Gaussian pulse, of the form

$$src(t) = -8\pi^2\,\tau^{-2}\left(t - \frac{1}{2}\tau\right) \exp\left[-4\pi^2\left(\frac{t}{\tau} - \frac{1}{2}\right)^2\right] \quad (1)$$

where the frequency content of this source function is controlled by τ. This time function is a full-cycle pulse (shown in Fig. 1a). The impulse responses are computed for a given layered crustal model and a ray parameter using Kennett's reflectivity matrix approach (Kennett, 1983). The calculation yields a full response including mode conversions. For our purposes, we consider the response at the free surface.

Figure 1 shows the procedure of calculating synthetic seismograms from two crustal models and the frequency-dependent crustal corrections obtained from waveform cross correlation. One of the models is the IASP91 (Kennett and Engdahl, 1991). The other is the crustal structure beneath the Global Seismic Network (GSN) station DGAR (7.412° S, 72.453° E), an ocean island site with a relatively thin crust, from CRUST2.0 (Bassin *et al.*, 2000). For simplicity, the first four layers in CRUST2.0 (water, ice, and soft and hard sediment) are not included in the calculations. This is reasonable because permanent seismic stations are usually set up on bedrocks. The thickness, V_p, V_s, and density of each layer in the two crustal models are shown in Figure 1b. Figure 1c shows the calculated impulse responses of these two models to an incident *P* wave by the reflectivity matrix method (Kennett, 1983). The impulse responses are then convolved with the source time function (Fig. 1a) to generate synthetic seismograms (Fig. 1d). To find the frequency dependence of the travel-time differences between the two models, we filtered these seismograms using the high-, intermediate-, and low-frequency bands as in Hung *et al.* (2004) (0.5–2, 0.1–0.5, and 0.03–0.1 Hz, respectively). Relative travel-time delays or crustal corrections for the three frequency bands are then measured from the cross correlation of the two filtered seismograms. As shown in Figure 1e, while the travel-time differences are nearly identical for high- and intermediate-frequency signals, the arrival at DGAR at the low frequency is much earlier (by an additional 0.65 sec) than at the intermediate and high frequencies, due to the overlap of crustal reverberations with the long-period direct arrivals and the smaller separation between the reverberations and the direct arrival at the station above a thin crust.

To see how variations in crustal thickness alone affect the travel times measured by waveform cross correlation, we systemically generated crustal models with different crustal thicknesses and repeated the preceding procedure to calculate the corrections relative to the IASP91 model. In this experiment, the crust is a two-layer model, in which the thickness of each layer is increased or decreased by the same

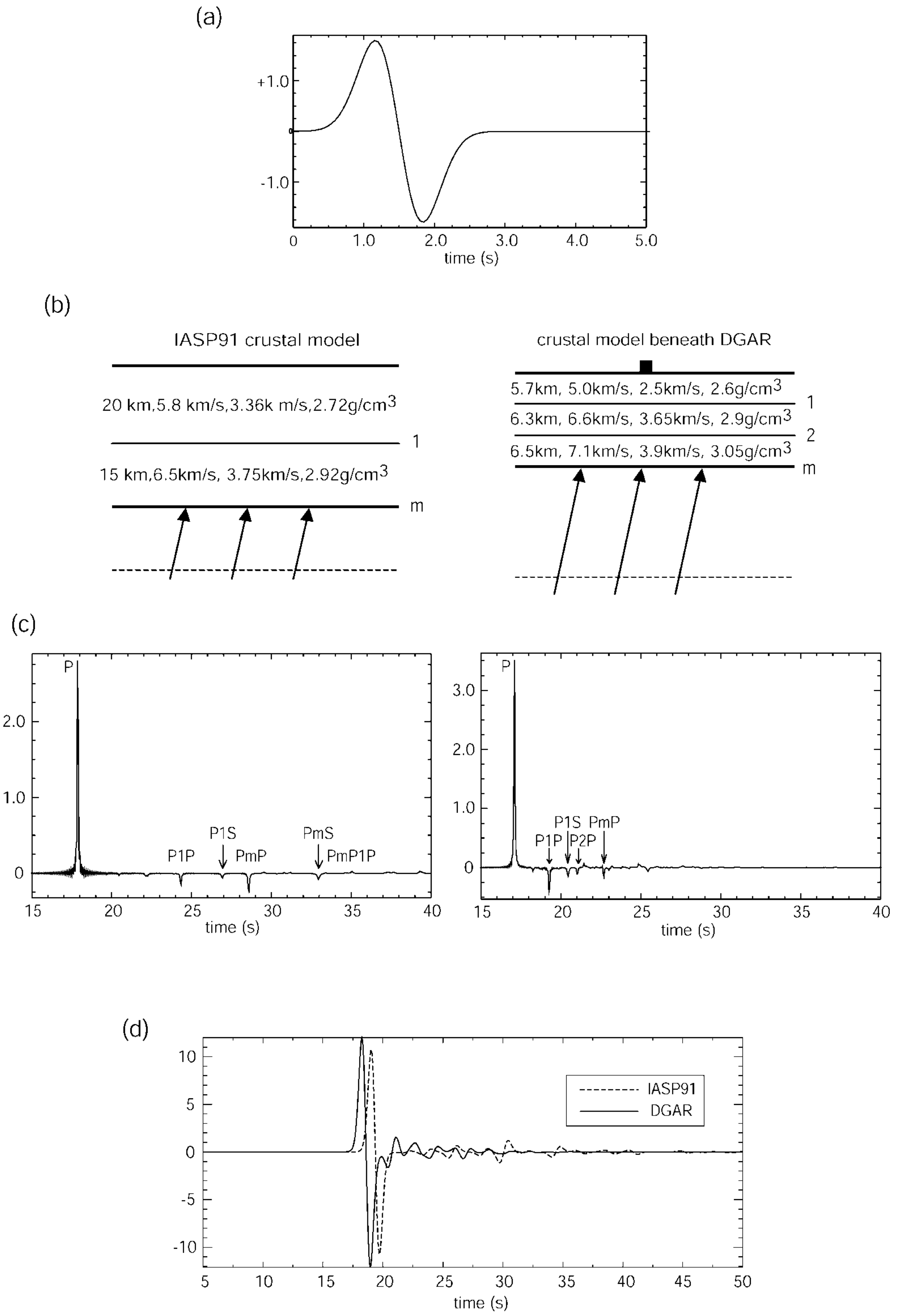

Figure 1. Procedure to generate synthetic seismograms on the vertical component for frequency-dependent crustal correction. (a) Source time function. The power spectrum of this example peaks at about 1 Hz and has energy between 0.001 and 2 Hz. (b) The IASP91 crustal model and a three-layer crustal model beneath the DGAR station from CRUST2.0 (Bassin *et al.*, 2000). Values within layers are thickness, V_p, V_s, and density, respectively. (c) Responses of the IASP91 model and the DGAR crustal model. The major reverberation phases are marked. *PdP* (*PdS*) stands for a *P* wave reflected at the surface and then reflected (converted to *S*) at the discontinuity *d* (1, 2, or the Moho). (d) Synthetic seismograms obtained from the convolution of the source time function and the crustal responses. (e) Bandpass-filtered seismograms for the IASP91 (dashed) and DGAR crust, and travel-time shifts between them measured by cross correlations. (*continued*)

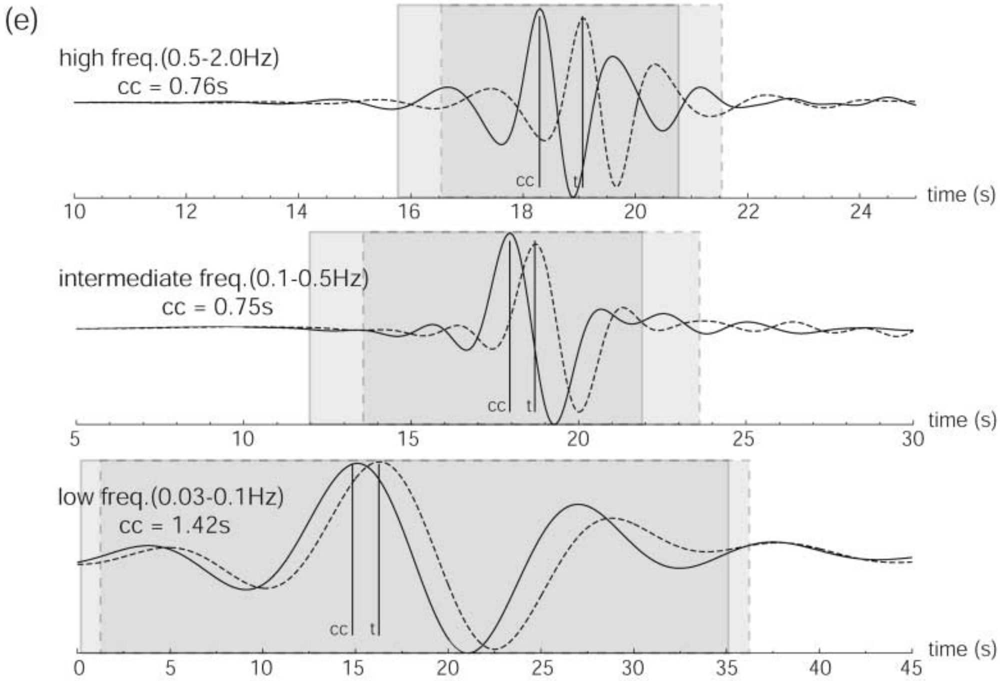

Figure 1. (continued). "*t*" marks the peak of seismograms from the IASP91 model, which is also the cross-correlation reference time; "cc" is the travel-time shift of the two seismograms measured from cross correlation (i.e., crustal correction). Shaded portions with dashed (IASP91) and solid (DGAR) frames indicate the windows for cross correlation. The crustal correction from the ray theory is 0.64 sec, and the ray parameter in this experiment is 0.06 sec/km. The difference between the value predicted by the ray theory and those obtained from waveform crosscorrelation is attributable to the large reverberation from the shallow crust beneath DGAR (*P1P*).

amount incrementally while all other parameters are kept the same as those in IASP91. Figure 2 shows the relationship between the crustal thickness and corrections. Corrections for low-, intermediate-, and high-frequency signals differ when the crustal thickness is less than that of IASP91 (35 km), with the most significant differences in the thickness range of 6–24 km. For the crust with a thickness near or greater than 35 km, the separation between the main reverberation phase (*PmP*) and the direct arrival is greater than 11 sec, sufficiently large that the reverberation does not overlap with the direct arrival and thus does not affect the measured travel times.

To see how internal layering affects the travel time measured by waveform cross correlation, we did a similar experiment with a more complex, three-layer crustal model (Fig. 3). Velocities and densities for this crust model are derived from the average values of the crustal structure beneath 180 eastern Eurasia stations from CRUST2.0 (water, ice, and sediment layers are also excluded), though we arbitrarily fix the thickness of each layer to be one third of the total crustal thickness. These parameters are shown in Table 1. Unlike in Figure 2, the frequency dependence in travel times does not disappear when the crustal thickness is equal to, or larger than that of the reference model (35 km). This is attributable to reverberations in the shallow crust in the three-layer model. So in addition to crustal thickness, the internal layering in the crust, in particular, the strong reflection in the shallow crust, may also have a significant effect on the waveforms and thus the travel times measured by waveform cross correlation.

The preceding synthetic experiments illustrate that, for travel times measured by waveform cross correlation, the effects of crustal reverberations are frequency dependent and must be taken into consideration in tomographic inversions. Crustal corrections calculated simply from ray theory for the direct arrival may leave large biases in the travel times of low-frequency waves and even short-period waves if strong reflectors exist in the shallow (depth <5 km) crust. Since most of the oceanic crust and a significant portion of the continental crust have a thickness within the range of 5 to 30 km, this bias in travel times may significantly degrade the resolution of the mantle structure in seismic tomography (van der Hilst and de Hoop, 2005). Frequency-dependent crustal corrections should be applied in FFST and other studies using low-frequency seismic records.

Practical Considerations

If an accurate crustal structure is available, the effect of crustal reverberations on waveforms can be removed by deconvolving the crustal response from the observed seismograms. The crustal corrections calculated from ray theory

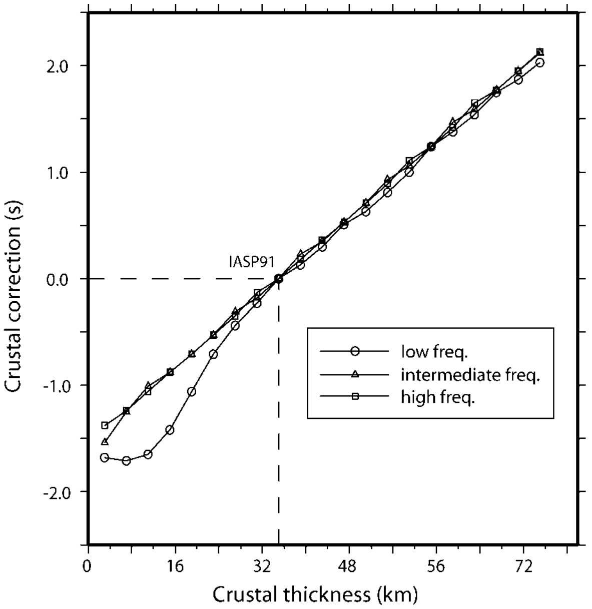

Figure 2. Effect of the crustal thickness on crustal corrections for the high- (0.5–2.0 Hz), intermediate- (0.1–0.5 Hz), and low- (0.03–0.1 Hz) frequency signals. The crust is a two-layer model with the same V_p, V_s, and density as those of IASP91. The thicknesses of the upper and lower crust are increased or decreased by the same amount in each calculation. The source time function is shown in Figure 1a.

can then be used properly for signals at all frequencies. However, this approach may not be practical since the deconvolution process is sensitive to the response, which requires a very accurate crustal model (Obayashi *et al.*, 2004).

Crustal corrections can also be approximated without the deconvolution of recorded waveforms by following the steps in Figure 1. In practice, this may also be achieved by calculating the impulse response of the crustal model directly, and filtering the response within the specified frequency bands. Real seismic records may have a higher energy toward the low-frequency end of the selected frequency band or vice versa. Thus real data may have a spectrum that is somewhat different from the impulse response, whose power spectrum is flat. This mismatch between the spectra of real records and the impulse response may introduce errors into the crustal corrections for travel times measured by waveform cross correlation. Our synthetic experiments show, however, that this error is likely negligible with narrow frequency bands. Figure 4 shows the difference between the correction obtained from synthetic seismograms with a known source time function (cc1) and that directly from the impulse response of the crust (cc2). We conducted this synthetic experiment for two sets of crustal models and several different source time functions having various power spectra. For the three frequency bands and all crustal models with different thicknesses, most of the differences between the two approaches are less than one sampling interval (0.05 sec), and the biggest one is 0.08 sec. This result suggests that, to first order, the crustal corrections within individual frequency bands are not very sensitive to the spectrum of the incoming wave and one may choose to use corrections measured directly from impulse responses to approximate those for observed waveforms.

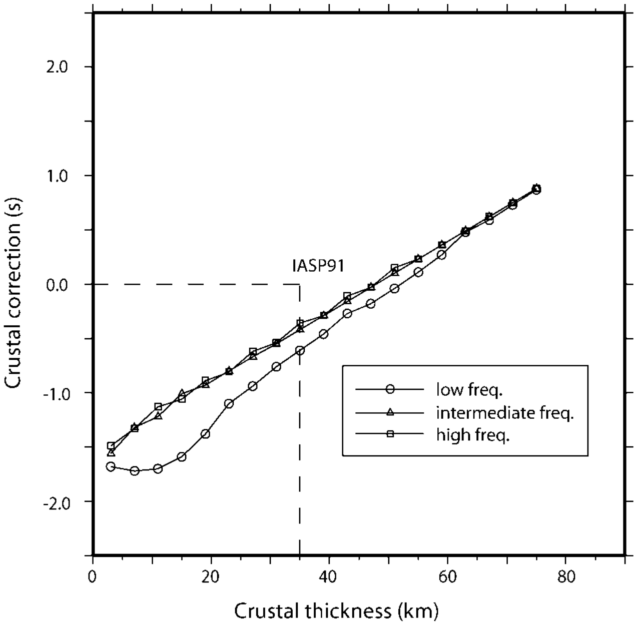

Figure 3. Effects of the crustal thickness and the internal layering on crustal corrections for the high- (0.5–2.0 Hz), intermediate- (0.1–0.5 Hz), and low- (0.03–0.1 Hz) frequency signals. The crust is a three-layer model with V_p, V_s, and density being the mean values of the crust beneath seismic stations in eastern Eurasia from CRUST2.0 (layer 5, 6, and 7) (Bassin *et al.*, 2000). The thickness of each layer is one third of the total crustal thickness. The average *P*-wave crustal velocity (6.55 km/sec) is higher than that in IASP91 (6.08 km/sec). The source time function is shown in Figure 1a.

Table 1
Average Crustal Structure beneath Seismic Stations in Eastern Eurasia* from CRUST2.0

	V_p (km/sec)	V_s (km/sec)	Density (g/cm^3)
Upper crust	5.97	3.39	2.71
Middle crust	6.55	3.67	2.88
Lower crust	7.13	3.95	3.06

*Stations are within the range of (20° S to 60° S, 60° E to 160° E).

With the preceding approximations, a first-order crustal correction can be obtained through the following steps:

1. Calculate the ray parameter based on the station and earthquake locations.
2. Calculate the responses of the crustal model beneath the station and the reference model for the ray parameter.

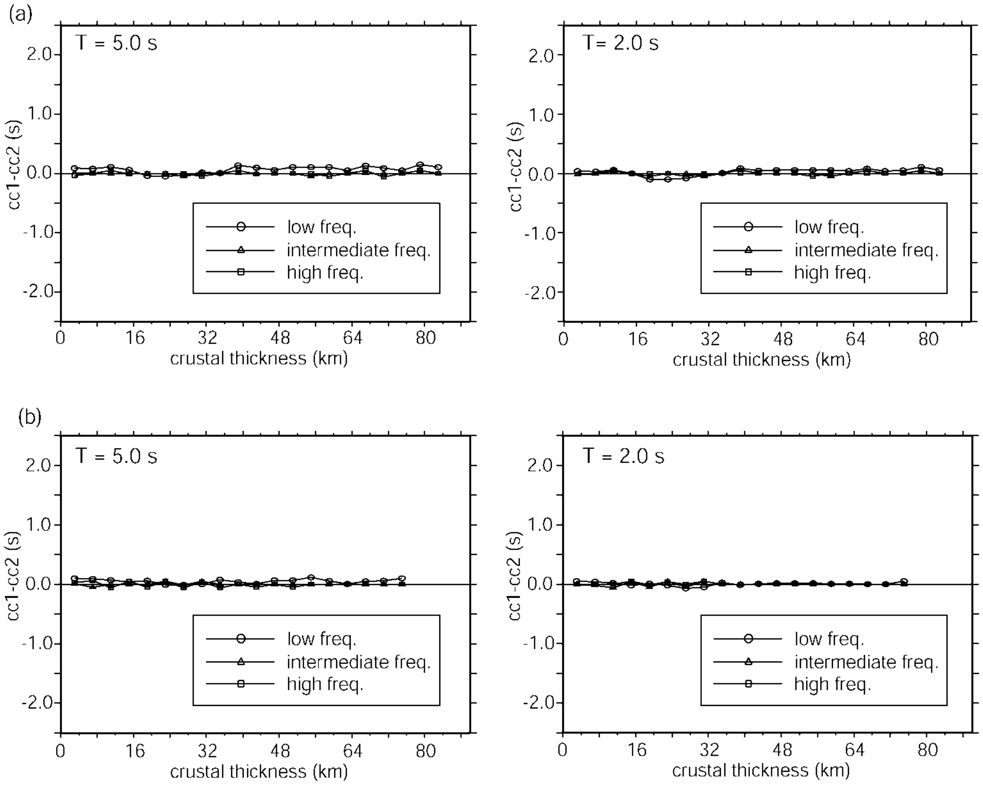

Figure 4. Differences between crustal corrections from synthetic seismograms (cc1) and those from impulse responses (cc2) for the high- (0.5–2.0 Hz), intermediate- (0.1–0.5 Hz), and low- (0.03–0.1 Hz) frequency bands. (a) The two-layer, IASP91-type crust. (b) The three-layer crust, as shown in Table 1. "T" is the apparent period of the source time source (τ) in equation (1).

3. Filter the responses in the same frequency ranges as those of real data.
4. Cross-correlate the two filtered responses from the reference model and the model for a station to measure the correction for a specified frequency band.
5. Apply the correction to the corresponding travel time of the observed waveform at the station.

To get a quantitative estimate of the magnitude of frequency-dependent crustal corrections in a real-world situation, we applied this crust-correction procedure to broadband seismograms recorded at stations in the western Pacific. The crustal models beneath these stations are from CRUST2.0 (Bassin *et al.*, 2000). Figure 5 shows an example of the effect of the frequency-dependent crustal correction on travel time shifts, in which the magnitude of crustal correction is comparable to the relative delays measured by cross correlation and the difference between the high- and low-frequency corrections is as much as 25% of the travel-time delays.

There are two other assumptions in the previous examples that one may consider in the crustal correction. First, the uppermost mantle velocity affects the impedance contrast at the Moho and thus has an effect on the waveform of the crustal reverberation and on the crustal correction. In many cases (e.g., the global crustal model CRUST2.0), the uppermost mantle velocity is unavailable. One has to assume a velocity for the uppermost mantle. To assess how this assumption affects the crustal correction, we changed the uppermost mantle velocity and compared crustal corrections with that based on the IASP91 velocity. A ±3.7% variation in the uppermost mantle velocity (7.75–8.35 km/sec) causes a very small difference (0.035 sec) in the measured low-frequency travel times. Therefore, to first order, the effect of the uppermost mantle velocity is negligible.

Second, we assume flat crustal interfaces in these calculations of the crustal response. The real crust has 2D or 3D variations in velocity and interfaces, which have more complex influences on the waveforms of recorded broadband signals. For regions having well-constrained 2D or 3D crustal models, the crustal responses can be calculated with other techniques (e.g., Komatitsch and Vilotte, 1998; Frederiksen and Bostock, 2000; Kang and Baag, 2004).

This paper focuses on *P* waves. We note that teleseismic *S* waves are usually observed at periods of several seconds and longer. Depending on the frequency of the *S* arrivals and the crustal structure, reverberations of *S* waves in the crust may also overlap with the direct *S* arrival and thus affect the travel times measured by waveform cross correlation. The

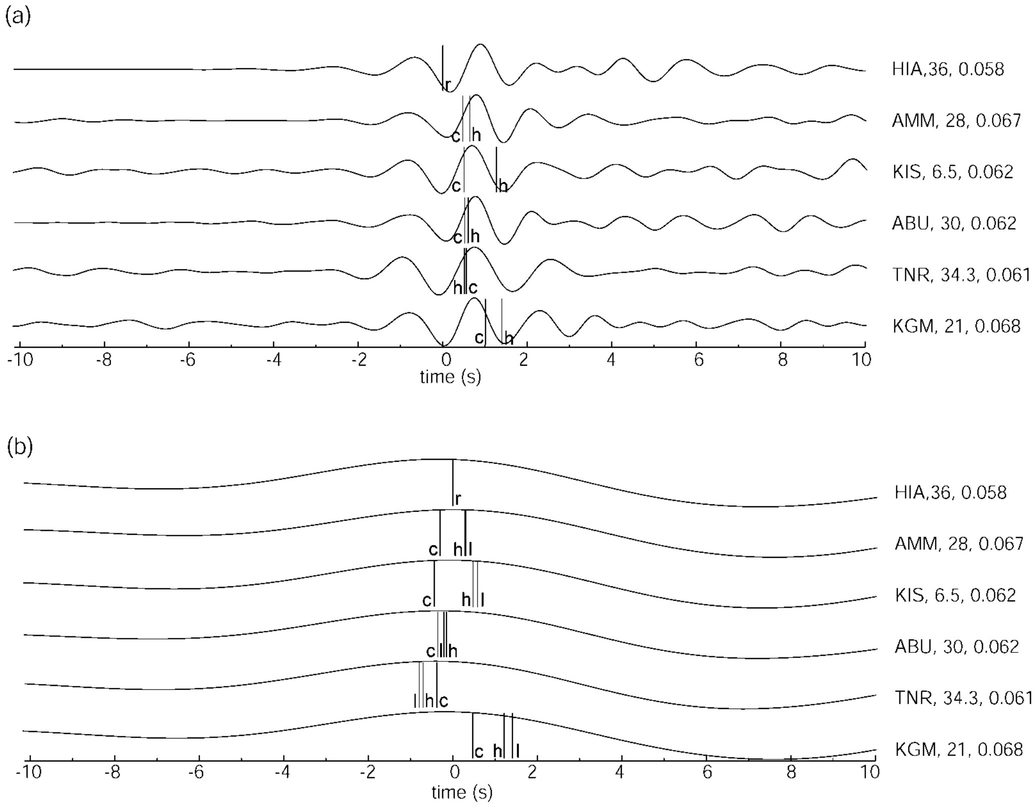

Figure 5. The filtered high- (0.5–2.0 Hz) (a) and low- (0.03–0.1 Hz) (b) frequency seismograms at six stations in the western Pacific. Seismograms are aligned according to the time shifts determined from waveform cross correlation. The vertical bars mark the time shifts (relative to the “r” bar in the first trace) calculated from the waveform cross correlation (“c”). “h” and “l” represent the adjusted time shifts after the crustal corrections estimated from the impulse response in the high- and low-frequency bands, respectively. In low-frequency seismograms (b), the time shifts with crustal corrections calculated from the high-frequency impulse response (“h”) are also shown for comparison with “l”. Values after station names are the thickness of the crust beneath the station in kilometers (Bassin *et al.*, 2000) and the ray parameter in seconds per kilometer The earthquake occurred at 02:45:59 on 7 September 2001, and the epicenter was at (13.16° S, 97.30° E).

frequency-dependent *S* crustal correction can be determined in the same way as outlined for *P* waves.

Conclusions

Through a series of synthetic experiments, we demonstrate that the effects of crustal structure on travel times measured by waveform cross correlation are frequency dependent. The difference in crustal correction between high- and low-frequency arrivals could reach as large as 0.65 sec for a relatively thin crust and crust with strong shallow reverberations. As a result, this frequency dependence in travel times measured by waveform cross correlation cannot be ignored in finite-frequency tomography or any tomography using low frequency or broadband body waves. The frequency-dependent crustal correction can be approximated, to first order, by cross-correlating the impulse responses of a crust model filtered in a narrow frequency band.

References

Allen, R. M., G. Nolet, W. J. Morgan, K. Vogfjord, B. H. Bergsson, P. Erlendsson, G. R. Foulger, S. Jakobsdottir, B. R. Julian, M. Pritchard, S. Ragnarsson, and R. Stefansson (2002). Imaging the mantle beneath Iceland using integrated seismological techniques. *J. Geophys. Res.* **107,** 2325, doi 10.1029/2001JB000595.

Bassin, C., G. Laske, and G. Masters (2000). The current limits of resolution for surface wave tomography in North America, *EOS Trans. AGU* **81,** F897.

Beck, S., G. Zandt, S. C. Myers, T. C. Wallace, P. G. Silver, and L. Drake (1996). Crustal-thickness variations in the central Andes, *Geology* **24,** 407–410.

Dahlen, F. A., S.-H. Hung, and G. Nolet (2000). Frechet kernels for finite frequency traveltimes. I. Theory, *Geophys. J. Int.* **141,** 157–174.

Dawson, P. B., J. R. Evan, and H. M. Iyer (1990). Teleseismic tomography of the compressional wave structure beneath the Long Valley region, *J. Geophys. Res.* **95,** 11,021–1,050.

Evans, J. R., and U. Achauer (1993). Teleseismic velocity tomography using the ACH-method: Theory and applicaiotn to continental-scale studies, in *Seismic Tomography: Theory and Practise,* K. M. Iyer and K. Hirahara (Editors), Chapman and Hall, London, 319–360.

Foulger, G. R., M. J. Pritchard, B. R. Julian, J. R. Evans, R. M. Allen, G. Nolet, W. J. Morgan, B. H. Bergsson, P. Erlendsson, S. Jakobsdottir, S. Ragnarsson, R. Stefansson, and K. Vogfjord (2001). Seismic tomography shows that upwelling beneath Iceland is confined to the upper mantle, *Geophys. J. Int.* **146,** 504–530.

Frederiksen, A. W., and M. G. Bostock (2000). Modeling teleseismic waves in dipping anisotropic structure, *Geophys. J. Int.* **141,** 401–412.

Hung, S-H, Y. Shen, and L.-Y. Chiao (2004). Imaging seismic velocity structure beneath the Iceland hot spot: a finite frequency approach, *J. Geophy. Res.* **109,** doi 10.1029/2003JB002889.

Kang, T. S., and C. E. Baag (2004). An efficient finite-difference method for simulating 3D seismic response of localized basin structures, *Bull Seism. Soc. Am.* **94,** 1690–1705, doi 10.1785/012004016.

Kennett, B. L. N. (1983). *Seismic Wave Propagation in Stratified Media,* Cambridge University Press, New York.

Kennett, B. L. N., and E. R. Engdahl (1991). Traveltimes for global earthquake location and phase identification, *Geophys. J. Int.* **105,** 429–465.

Keyser, M. J., R. R. Ritter, and M. Jordan (2002). 3D shear-wave velocity structure of the Eifel plume, Germany, *Earth Plant. Sci. Lett.* **203,** 59–82.

Kissling, E. (1993). Deep structure of the Alps—what do we really know? *Phys. Earth Planet. Interiors* **79,** 87–112.

Komatitsch, D., and J. P. Vilotte (1998). The spectral-element method: an efficient tool to simulate the seismic response of 2D and 3D, geological structures, *Bull. Seism. Soc. Am.* **88,** 368–392.

Martin, M., and J. R. R. Ritter and the CALIXTO Working Group (2005). High-resolution teleseismic body-wave tomography beneath SE Romania. I. Implications for three-dimensional versus one-dimensional crustal correction strategies with a new crustal velocity model, *Geophys. J. Int.* **162,** 448–460, doi 10.1111/j.1365-246X.2005.02661.x.

Obayashi, M., D. Suetsugu, and Y. Fukao (2004). PP-P differential traveltime measurement with crustal correction, *Geophys. J. Int.* **157,** 1152–1162.

Shen, Y., and S.-H. Hung (2004). Ridge-like upwelling in the uppermost lower mantle beneath eastern Africa from finite-frequency seismic tomography (abstract), *EOS Trans. AGU* **85,** no. 47 (Fall Meet. Suppl.), U41A-0720.

VanDecar, J. C., and R. S. Crosson (1990). Determination of teleseismic relative phase arrival times using multi-channel cross-correlation and least squares, *Bull. Seism. Soc. Am.* **80,** 150–169.

VanDeCar, J. C., D. E. James, and M. Assumpcao (1995). Seismic evidence for a fossil mantle plume beneath South America and implications for plate driving forces, *Nature* **378,** 27–31.

van der Hilst, R., and M. V. de Hoop (2005). Banana-doughnut kernels and mantle tomography, *Geophys. J. Int.* **163,** 956–961.

Waldhauser, F., R. Lippitsch, E. Kissling, and J. Ansorge (2002). High-resolution teleseismic tomography of upper-mantle structure using an *a priori* three-dimensional crustal model, *Geophys. J. Int.* **150,** 403–414.

Webb, S. C. (1998). Broadband seismology and noise under the ocean, *Rev. Geophys.* **36,** 105–142.

Wilcock, W. S. D., S. C. Webb, and I. T. Bjarnason (1999). The effect of local wind noise on seismic noise near 1 Hz at the MELT site and in Iceland, *Bull. Seism. Soc. Am.* **89,** 1543–1557.

Wolfe, C. J., I. Th. Bjarnason, J. C. VanDecar, and S. C. Solomon (1997). Seismic structure of the Iceland mantle plume, *Nature* **385,** 245–247.

Yang, T., Y. Shen, S. van de Lee, S. Solomon, and S.-H. Hung (2006). Upper mantle structure beneath the Azores hotspot from finite frequency seismic tomography, *Earth Planet. Sci. Lett.* **250,** 11–26, doi 10.1016/j.epsl.2006.07.031.

Graduate School of Oceanography
University of Rhode Island
Narragansett, Rhode Island 02882

Manuscript received 19 February 2006.

APPENDIX II.

Finite Frequency Tomography in Southeastern Tibet

by Yong Ren and Yang Shen

JOURNAL OF GEOPHYSICAL RESEARCH, VOL. 113, B10316, doi:10.1029/2008JB005615, 2008

Finite frequency tomography in southeastern Tibet: Evidence for the causal relationship between mantle lithosphere delamination and the north–south trending rifts

Yong Ren[1] and Yang Shen[1]

Received 2 February 2008; revised 14 July 2008; accepted 28 July 2008; published 28 October 2008.

[1] While several mechanisms have been suggested to explain the evolution of the Tibetan Plateau, observational constraints on the deep lithospheric processes have been sparse, and previous seismic studies were mostly along profiles perpendicular to the collision front of the Indian and Eurasian plates. In this study, we show tomographic evidence for the delamination of the mantle lithosphere beneath southeastern Tibet, a process in which the entire mantle lithosphere peels away from the crust along the Moho and thus is a mechanism for rapid thinning of the lithosphere. Our P and S wave velocity models show the presence of a low-velocity anomaly in the crust and upper mantle down to $\sim$300 km depth beneath a north–south trending rift zone in southeastern Tibet. This low-velocity anomaly is situated above a tabular, high-dipping-angle, high-velocity anomaly that extends into the upper mantle transition zone. The V_P/V_S ratio of this high-velocity anomaly suggests that temperature variations are not the only cause of the anomaly and a highly melt-depleted mantle is required. These observations suggest a causal relationship between the delamination of mantle lithosphere and the formation of the north–south trending rift in southeastern Tibet.

Citation: Ren, Y., and Y. Shen (2008), Finite frequency tomography in southeastern Tibet: Evidence for the causal relationship between mantle lithosphere delamination and the north–south trending rifts, *J. Geophys. Res.*, *113*, B10316, doi:10.1029/2008JB005615.

1. Introduction

[2] Since the collision of India and Eurasia about 50 Ma ago, at least 2000 km of convergence has been accommodated by thickening the crust and elevating the Himalayan-Tibetan Plateau [*Yin and Harrison*, 2000]. The region has been strongly deformed through a combination of thrust, extension, and strike-slip faulting. Among the various styles of deformation, north–south and northeast–southwest trending rift zones, which indicate generally east–west extension, are enigmatic features. They are distributed mainly in the southern and central Tibetan Plateau [*Molnar and Tapponnier*, 1978; *Armijo et al.*, 1986, 1989; *Rothery and Drury*, 1984], where topography reaches high altitudes. Field observations indicate that the magnitude of this extension is small (<1%) [*Armijo et al.*, 1986] and rifting in southern and central Tibet started about 13.5–14 Ma ago [*Yin et al.*, 1994; *Coleman and Hodges*, 1995; *Harrison et al.*, 1995; *Blisniuk et al.*, 2001].

[3] Whether the north–south trending rifts are shallow crustal features or a surface manifestation of a coherent deformation throughout the entire crust and mantle lithosphere is a key question in the continuing debate about the mechanisms that form the Tibetan Plateau [e.g., *Holt*, 2000; *Yin*, 2000]. The late Cenozoic east–west extension of the plateau is commonly attributed to gravitational collapse of the thickened crust [*Mercier et al.*, 1987; *Dewey*, 1988; *England and Houseman*, 1989; *Liu and Yang*, 2003], the consequence of a sharp increase in potential energy after an abrupt rise of the plateau due to convective removal of the lower mantle lithosphere [*England and Houseman*, 1989]. Numerical modeling indicates that the present high surface elevation and small regional topographic slope within the plateau require the removal of the underlying mantle lithosphere [*Jiménez-Munt and Platt*, 2006]. However, the time scale involved in the convective removal of the mantle lithosphere is uncertain because the viscosity is not well known. Numerical simulations by different authors show that the duration of the removal can vary drastically from 10 Ma to a few hundreds of million years, depending on the rheological parameters in the simulation experiments [*Davaille and Jaupart*, 1993; *Conrad*, 2000; *Houseman et al.*, 2000; *Morency et al.*, 2002]. The roughly concurrent onsets of tectonic processes in the surrounding regions have led to the suggestion of a rapid removal of the mantle lithosphere beneath Tibet at about 8 Ma ago [*Harrison et al.*, 1992; *Molnar et al.*, 1993].

[4] Observations that support the notion of a vertically coherent deformation of the lithosphere [*Tapponnier et al.*,

---

[1] Graduate School of Oceanography, University of Rhode Island, Narragansett, Rhode Island, USA.

Copyright 2008 by the American Geophysical Union.
0148-0227/08/2008JB005615$09.00

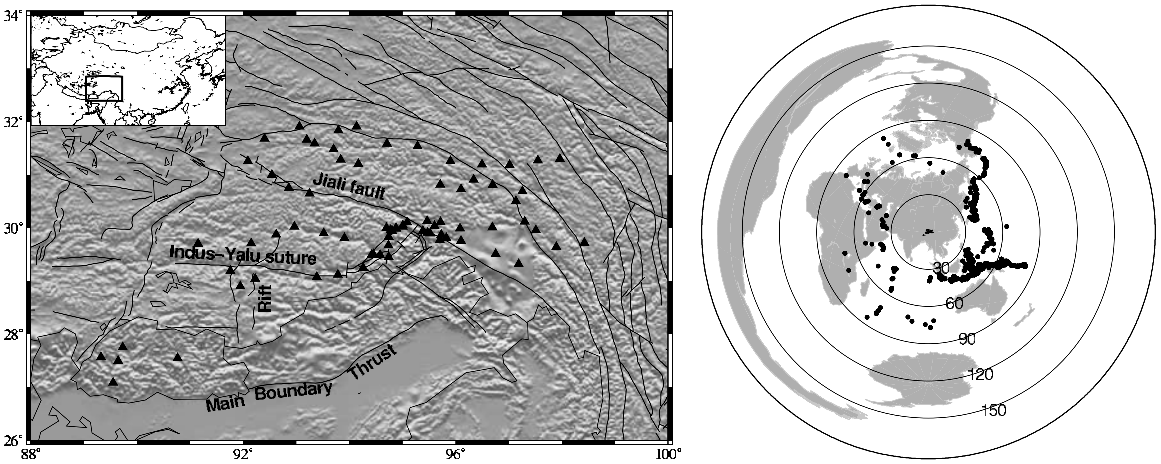

(a) Stations (b) Events

Figure 1. (a) Topographic map of southeastern Tibet with active faults in the region of the Himalayan Eastern syntaxis and the locations of the stations used in this study (triangles). (b) Distribution of the earthquakes (circles) used in this study. Triangles represent the stations used. Numbers are the distance in degrees to the center of the stations.

1982; *England and Houseman*, 1986] include the studies of earthquake focal mechanisms which show brittle east–west extension in the mantle directly beneath the north–south trending rifts [*Chen and Kao*, 1996; *Chen and Yang*, 2004] and the instability analysis of the spacing between the rifts [*Yin*, 2000]. On the other hand, the presence of a low-viscosity mid and lower crust may decouple deformation in the shallow crust from that in the mantle lithosphere [*Zhao and Morgan*, 1987; *Bird*, 1991; *Royden*, 1996]. Other explanations for the east–west extension in the Tibetan Plateau include the combination of the eastward extrusion of Tibet and strike-slip faulting along the Himalayan arc caused by oblique convergence between India and Eurasia [*Tapponnier et al.*, 1981; *Armijo et al.*, 1986; *McCaffery and Nabelek*, 1998; *Tapponnier et al.*, 2001], and the collisional stresses localized along the southern part of the Himalayan arc [*Kapp and Guynn*, 2004].

[5] Direct observational constraints on the crust and mantle structure beneath the rifts are needed to understand the east–west extension of the Tibetan Plateau and the dynamic processes that generate the rifts. In this paper, we present tomographic images of the lower crust and upper mantle beneath a north–south trending rift in the region of the Eastern Himalayan Syntaxis, which marks the eastern end of the Himalayan orogenic belt (Figure 1a). The results support the notion of the mantle control of the north–south trending rifts and suggest that delamination of the mantle lithosphere plays an important role in the rise of the plateau in the study area.

2. Data

[6] The data used in this study come from three sources in southeastern Tibet: (1) the Namche Barwa seismic experiment, which deployed a 50-station array of broadband seismometers and a 20-element array of short-period seismometers during 2003–2004 [*Sol et al.*, 2007], (2) the Global Seismic Network (GSN) station LSA, and (3) the broadband stations in the Bhutan experiment, which recorded concurrently with the Namche Barwa array in 2003 (Figure 1a). We used 695 events occurred during the operation period of the stations in 2003 and 2004, and with magnitude greater than 5.5 (Figure 1b). With the multichannel waveform cross correlation method [*VanDecar and Crosson*, 1990], we measured differential travel times of teleseismic *P* and *S* waves between different stations in short, intermediate, and long periods: 0.5–2.0, 0.1–0.5, and 0.03–0.1 Hz for *P* waves and, 0.1–0.5, 0.05–0.1, and 0.02–0.05 Hz for *S* waves. The *P* differential traveltimes are measured on vertical component seismograms and those of *S* on transverse components. In order to avoid the ambiguity of long-period phase arrivals in the triplication range and the effects of the core-mantle boundary, we have considered only data with epicentral distance between 34° and 81°.

[7] Our final data set consists of ∼36313 *P* (19,131, 10,090 and 7092 for short, intermediate, and long periods, respectively) and ∼15043 *S* differential traveltimes (6629, 6040, and 2374 for short, intermediate, and long periods, respectively), which are then utilized to invert for spatial variations in *P* and *S* wave velocity perturbations according to the 3-D finite frequency kernel formulation [*Dahlen et al.*, 2000; *Hung et al.*, 2004]. For the inversion, we used either the combination of data at all frequency bands, the combination of only high- and intermediate-frequency data and only the high-frequency data to test the reliability of different data. The different combinations yield similar results, though adding lower frequency data reduces the variance reduction of the final model. This is likely caused by the relatively larger errors in the long-period measurements. The tomographic models discussed in this paper come from the inversion of the high- and intermediate-frequency data. Figure 2a shows the average teleseismic differential traveltime residuals at each station for *P* and *S* waves. They are consistent with *P* and *S* wave velocity

a) Mean traveltime residuals

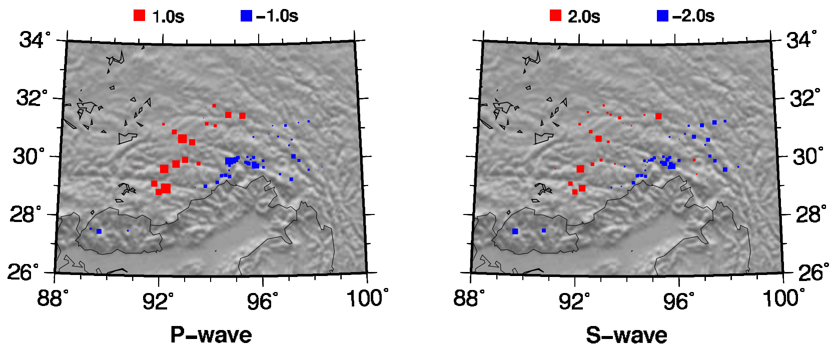

b) Station terms from inversion

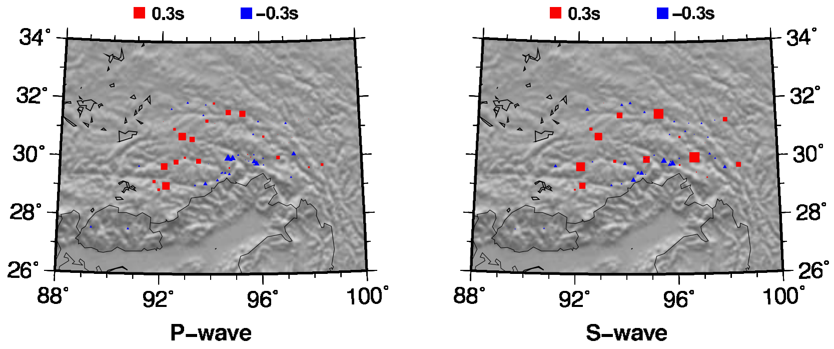

Figure 2. (a) Mean traveltime residuals at each station for (left) *P* wave and (right) *S* wave. Blue indicates an earlier than expected arrival; red indicates a later than expected arrival. Delay magnitude correlates linearly with the size of symbols. (b) Station terms for (left) *P* wave and (right) *S* wave, which are solved simultaneously in the inversion in order to absorb travel time fluctuations due to uncorrected shallow structures.

anomalies obtained from the inversion, discussed in sections 3–5.

3. Methodology

[8] Most of global and regional tomographic studies are based on ray theory, where seismic waves are assumed to have an infinite frequency and the arrival time of a body wave phase depends only upon the wave speed along the geometrical ray path between the source and receiver. However, because of wave front healing, scattering, and other diffraction effects, the traveltime of a finite frequency seismic wave is sensitive to a three-dimensional structure off the ray path [*Dahlen et al.*, 2000]. Using body wave ray theory in conjunction with the Born single-scattering approximation, *Dahlen et al.* [2000] derived the formulation of the Born-Fréchet kernels for a seismic phase, which expresses the influence of velocity perturbations upon a finite frequency travel time shift:

$$\delta t = \int\int\int_{\oplus} K(\mathbf{x})\delta c(\mathbf{x})/c(\mathbf{x})d^3\mathbf{x} \qquad (1)$$

where K is the 3-D Fréchet sensitivity kernel for a shift $\delta\, t$, measured by cross correlation of an observed pulse with its spherical Earth synthetics. It is expressed by the formulation [*Dahlen et al.*, 2000]

$$K = \frac{1}{2\pi c}\left(\frac{R}{c_r R' R''}\right)\frac{\int_0^\infty \omega^3 |s_{syn}(\omega)|^2 \sin(\omega\Delta T)d\omega}{\int_0^\infty \omega^2 |s_{syn}(\omega)|^2 d\omega} \qquad (2)$$

where $\Delta T = T' + T'' - T$ represent the difference in travel time for the path with a detour through a single point scatterer between the source and receiver (time $T' + T''$) relative to the corresponding direct ray path (time T); R, R' and R'' are geometrical spreading factors for the unperturbated ray, the forward source-to-scatterer ray and the backward receiver-to-scatterer ray, respectively. The power spectrum, $|s_{syn}|^2$, is for the synthetic seismograms used for cross correlation. Cross-correlating with synthetics in different bandwidths takes advantage of the frequency dependence of the traveltimes.

[9] In this study, we used the finite frequency seismic tomography, as described by *Hung et al.* [2004] and *Yang et al.* [2006], to retrieve the crustal and mantle structures beneath southeastern Tibet. Our measured data d_i of *P* and *S* differential travel times can be inverted to produce

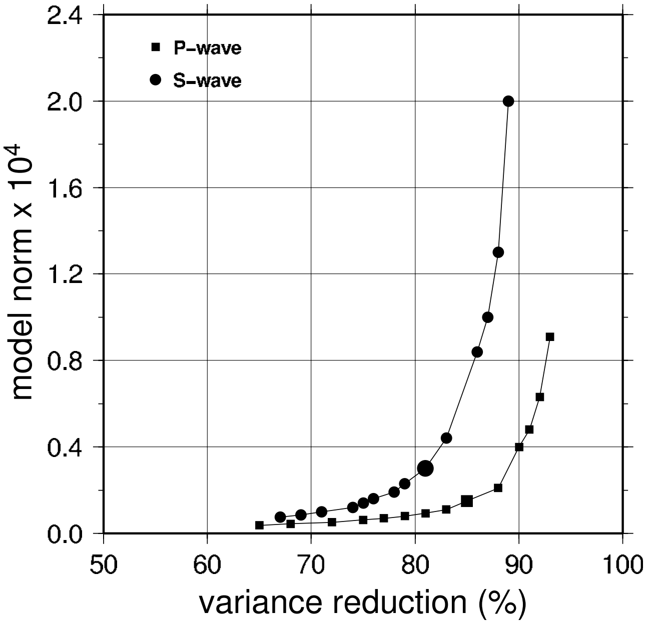

Figure 3. Trade-off curve between the model L2 norm and the data variance reduction for different values of the norm damping parameter for *P* and *S* waves. The larger square and dot represent parameters used to obtain the *P* and *S* velocity models discussed in this paper.

tomographic models of velocity perturbations using the following formulation:

$$d_i = \int_D g_i(\mathbf{x}) m(\mathbf{x}) d^3\mathbf{x} \tag{3}$$

where d_i, $i = 1 \ldots N$, represents the *i*th differential travel time data; **x** is the position vector in 3-D vector model space, *D*; and g_i represents the 3-D Fréchet sensitivity kernel relating to the data d_i with the model function $m(\mathbf{x})$.

[10] The crustal and mantle volume beneath the region of study is parameterized with regular 3D grids of 33 × 33 × 33 centered at (93.0°E, 30.0°N), and with a dimension of 18° in longitude, 14° in latitude, and 1200 km in depth. This results in a grid spacing of ~53 km in longitude, 46 km in latitude and ~40 km vertically. With this parameterization, equation (3) can thus be written as

$$d_i = G_{il} m_l \tag{4}$$

where d_i is the *i*th differential traveltime data, G_{il} represents the differential value of the integrated volumetric kernels contributing to the *l*th node, and m_l is the model parameter at the *l*th node. The inversion problem is resolved by the standard damped least square method [*Paige and Saunders*, 1982a, 1982b]:

$$\hat{\mathbf{m}} = \left(\mathbf{G}^T\mathbf{G} + \theta^2\mathbf{I}\right)^{-1}\mathbf{G}^T\mathbf{d} \tag{5}$$

where **I** is the identity matrix. The damping parameter θ is determined empirically through a space of variance reduction and the model norm represented by a trade-off curve (Figure 3). We choose the damping parameter that yields an optimum variance reduction and a relatively small model norm. The model discussed in this paper is obtained using a damping parameter that yields a variance reduction of ~85% for *P* wave and ~80% for *S* wave.

[11] The traveltime anomalies can be caused by crustal thickness, station elevations, and lateral velocity heterogeneities. Because the ray paths of teleseismic body waves are nearly vertical and crossing paths are rare at shallow depths, the shallow velocity structures are poorly constrained by relative traveltime data in the inversion. Therefore, a time correction is needed in order to reduce the tradeoff between crustal and mantle velocity heterogeneities in seismic tomography. To correct for the topographic effects, we have calculated the *P* and *S* phase time delays due to station elevations, using *P* and *S* ray parameters in the model iasp91 and a velocity of 5.8 km/s and 3.36 km/s for *P* and *S* waves, respectively. The measured differential traveltimes are then subtracted by the calculated *P* and *S* time delays for the topographic correction. To account for the thick crust beneath Tibet, we first replace the crust in the iasp91 model with the average crust structure beneath the stations from the crustal model CRUST2.0 [*Bassin et al.*, 2000]. Then, an additional free term at each station is incorporated into the inversion to absorb traveltime shifts caused by other shallow heterogeneity. Figure 2b shows that the simultaneously solved station terms yield a consistent pattern among *P* and *S* wave velocity models. The maximum difference between the station terms is ~0.36 s and ~0.42 s for *P* and *S* models, respectively.

4. Resolution Tests

[12] We performed different types of resolution tests to evaluate our data coverage and the ability of our inversion technique to recover the mantle structure. For this purpose, the synthetic traveltimes are computed by multiplying the G matrix (equation (4)) with different input velocity models: $\Delta t_{syn} = \mathbf{G} \cdot \Delta c_{synth}$. The inversion was then performed using the same damping parameter as in the inversion of real data. The resolution is considered good when input structures are well recovered, as illustrated in Figures 4–6. In the first set of the tests concentrating on the horizontal resolution, we conducted the checkerboard resolution tests using successively smaller-scale input anomalies with horizontal sizes of 200 km × 200 km, 150 km × 150 km, and 100 km × 100 km. In each case, the input models are composed by a velocity perturbation of ±2% for *P* wave and ±4% for *S* wave, which alternate horizontally (Figure 4a for P wave and Figure 5a for S wave). We estimated from the different tests that the resolution is good down to ~450 km depth for anomalies greater than and equal to 150 km, and ~300 km for 100-km-sized anomalies. The horizontal dimensions of the interpreted features in our tomographic model are about 150 km or more. In the second set of the tests for both horizontal and vertical resolutions, the input anomalies alternate both horizontally and vertically. These tests show that the minimum size of the anomaly which can be recovered vertically is ~120 km in the upper 400-km mantle (Figure 4b for *P* wave and Figure 5b for *S* wave).

[13] In order to obtain a quantitative assessment of the resolution tests, we calculated the correlation coefficient between the input and output models within the well

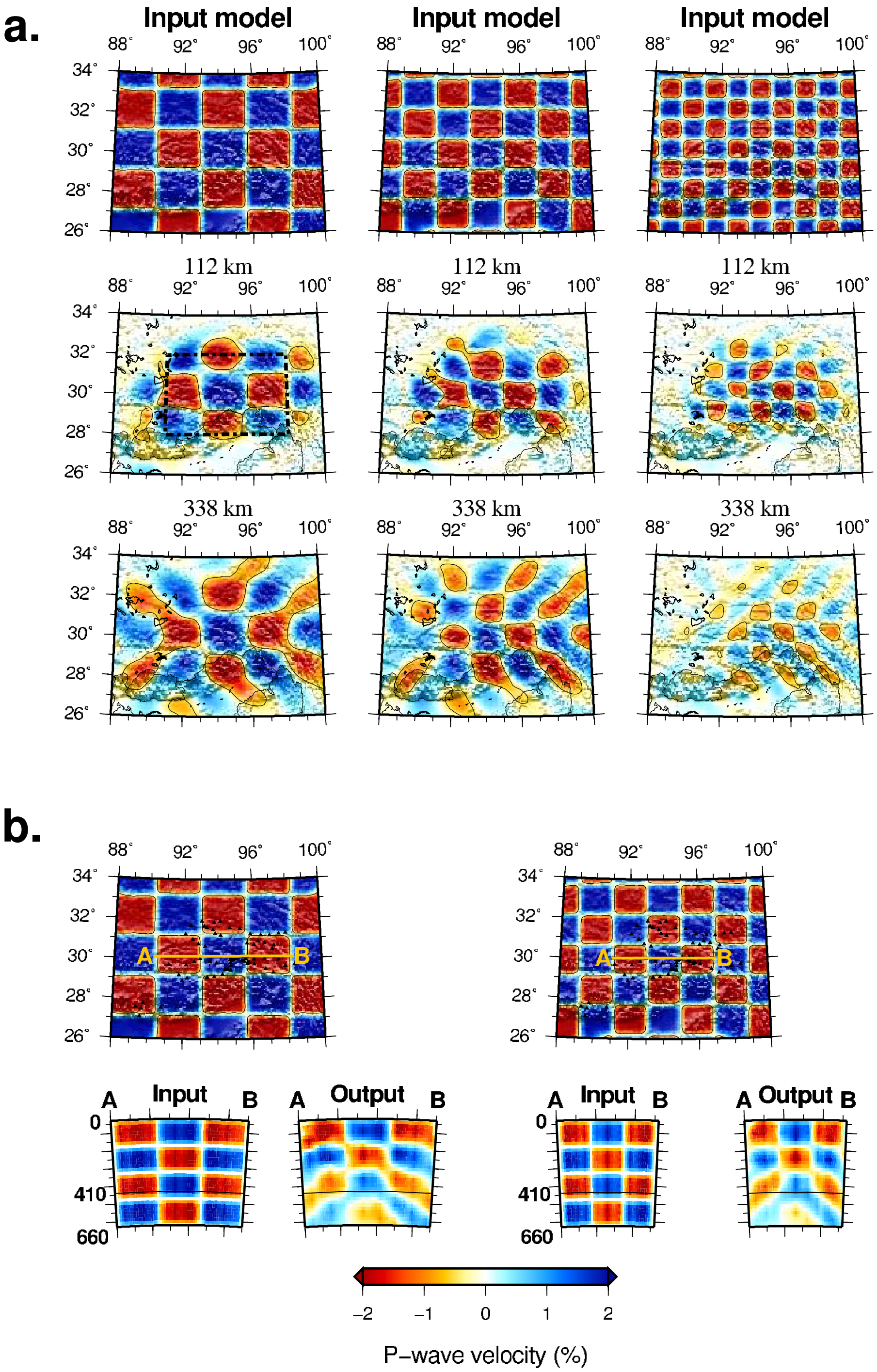
a.
Input model
Input model
Input model
112 km
112 km
112 km
338 km
338 km
338 km
88°
92°
96°
100°
34°
32°
30°
28°
26°
b.
A
B
Input
Output
0
410
660
−2
−1
0
1
2
P−wave velocity (%)

Figure 4. (a) Checkerboard resolution tests: (a) Horizontal slices of the input and retrieved *P* wave velocity models at depths 112 km and 338 km. The magnitudes of the input anomalies are ±2.0%; the sizes of the anomalies are (left) ~200 km × 200 km, (middle) ~150 km × 150 km and (right) ~100 km × 100 km. The rectangle with dashed lines on the horizontal slice at 112 km depth marks the area which we consider well resolved and used for Figure 6. (b) (left) Vertical slice along the path A-B through the input and retrieved *P* wave velocity model. The horizontal size of the anomalies is ~200 km × 200 km and the vertical size is ~120 km. (right) The same vertical slice for the input anomalies with the horizontal scale of ~150 km × 150 km and the vertical scale of ~120 km.

resolved area (rectangle with dashed lines in Figure 4a) as a function of depth (Figure 6a), as well as the standard deviation of the difference between the input and output models as a function of depth (Figure 6b), for the three cases of the input velocity anomalies above. For the *P* and *S* models with the two larger-sized anomalies, the correlation coefficients between the input and ouput models are very good in the upper 450 km depth (>0.9). The standard

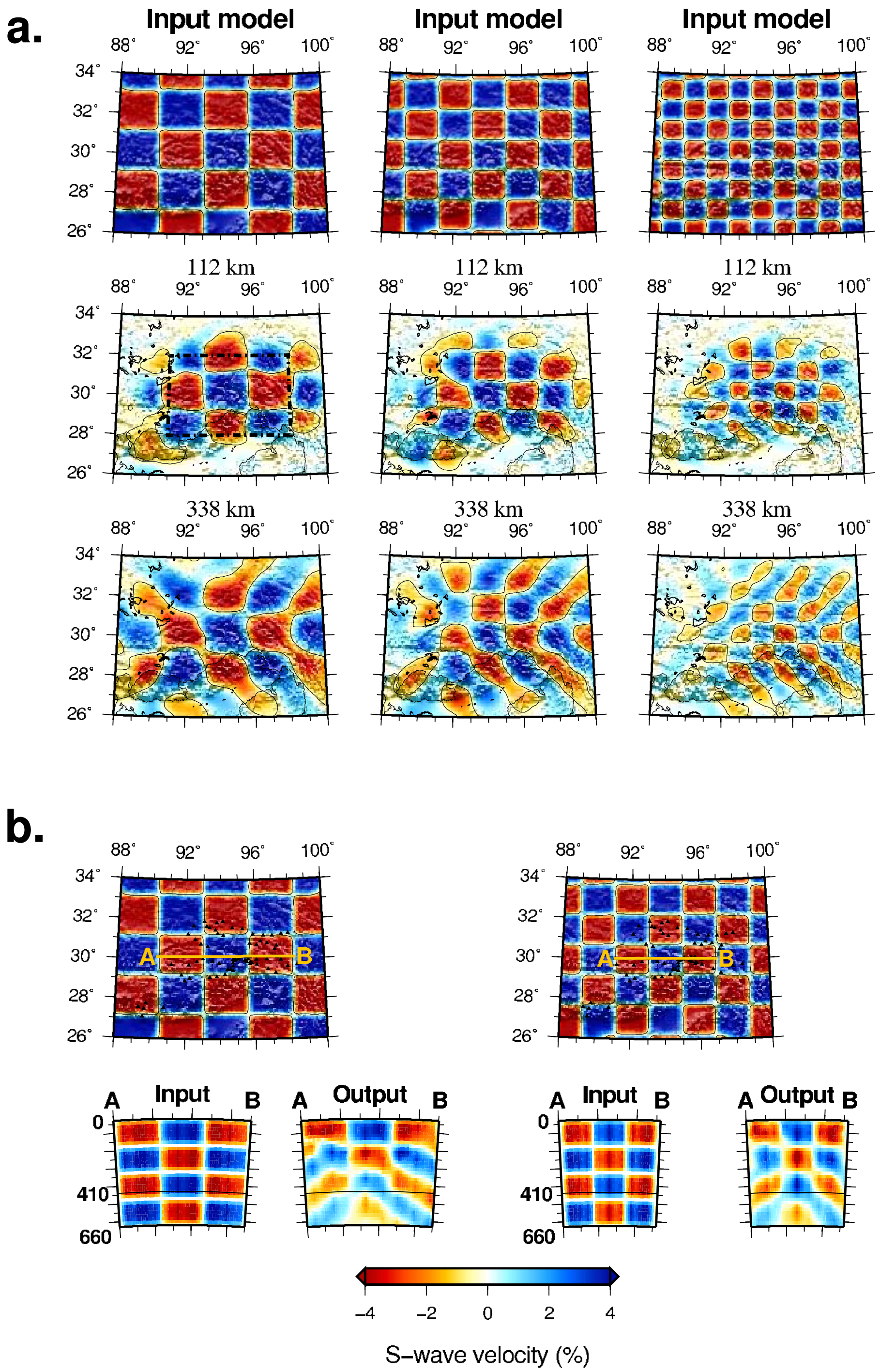
a.
Input model
Input model
Input model
112 km
112 km
112 km
338 km
338 km
338 km
88°
92°
96°
100°
34°
32°
30°
28°
26°
b.
A
B
Input
Output
0
410
660
–4
–2
0
2
4
S–wave velocity (%)

Figure 5. Checkerboard resolution tests: (a) Horizontal slices of the input and retrieved *S* wave velocity models at depths 112 km and 338 km. The magnitudes of the input anomalies are ±.0%; the sizes of the anomalies are (left) ~200 km × 200 km, (middle) ~150 km × 150 km and (right) ~100 km × 100 km. The rectangle with dashed lines on the horizontal slice at 112 km depth marks the area which we consider well resolved and used for Figure 6. (b) (left) Vertical slice along the path A-B through the input and retrieved *S* wave velocity model. The horizontal size of the anomalies is ~200 km × 200 km and the vertical size is ~120 km. (right) The same vertical slice for the input anomalies with the horizontal scale of ~150 km × 150 km and the vertical scale of ~120 km.

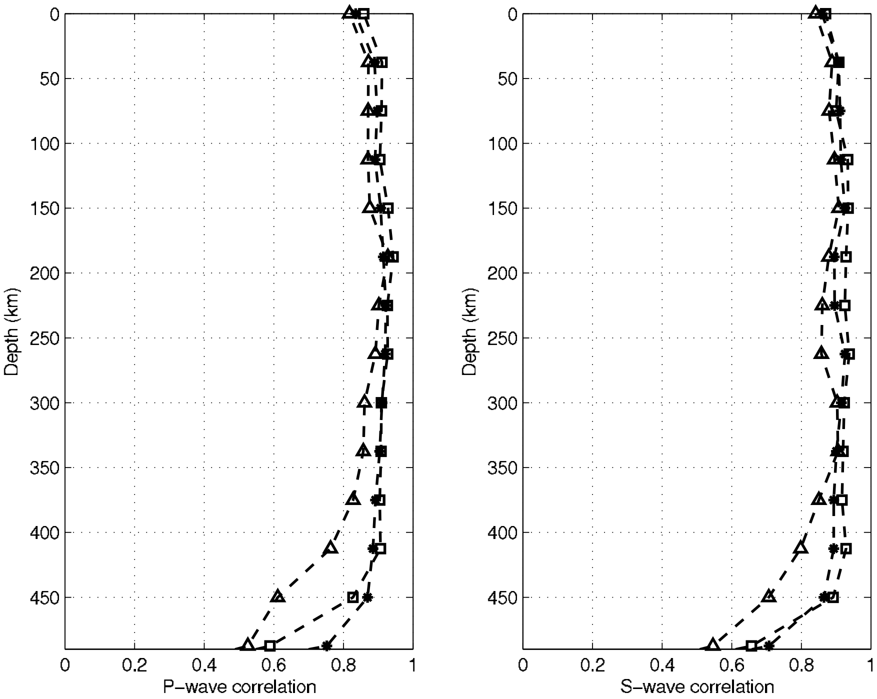

(a) Correlation coefficients between the input and output models

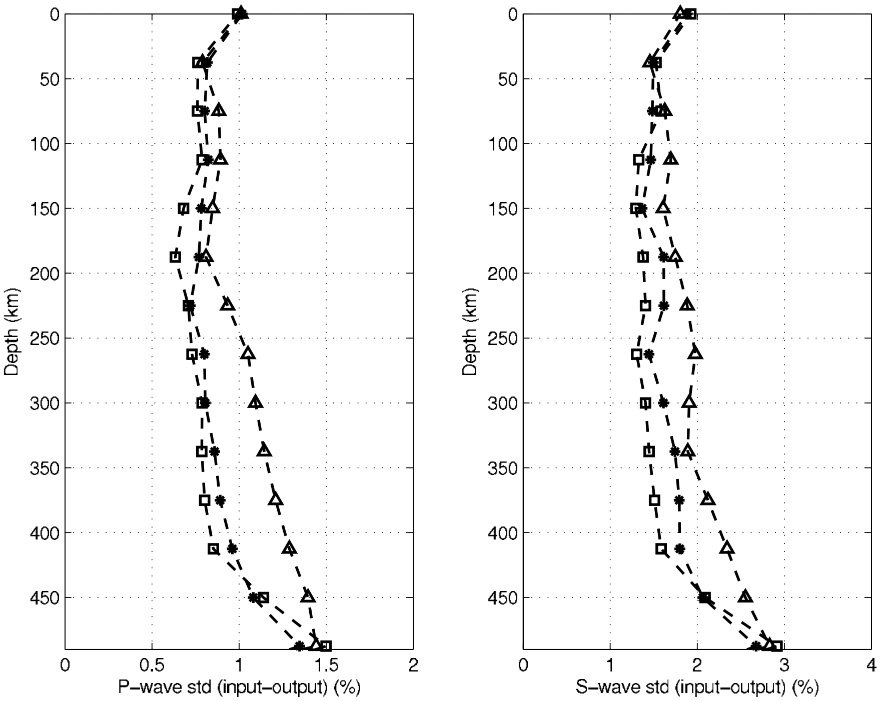

(b) Standard deviations of the amplitude between the input and output models

Figure 6. (a) Correlation coefficient between the input and output (left) *P* and (right) *S* models as a function of depth for the cases in which the sizes of the input anomalies are ~200 km × 200 km (line with squares), ~150 km × 150 km (line with stars), and ~100 km × 100 km (line with triangles). The calculations are for the area that we consider well resolved (rectangle with dashed lines in Figure 4a). (b) Standard deviation of the difference between the input and output models as a function of depth for the three cases of the input anomalies.

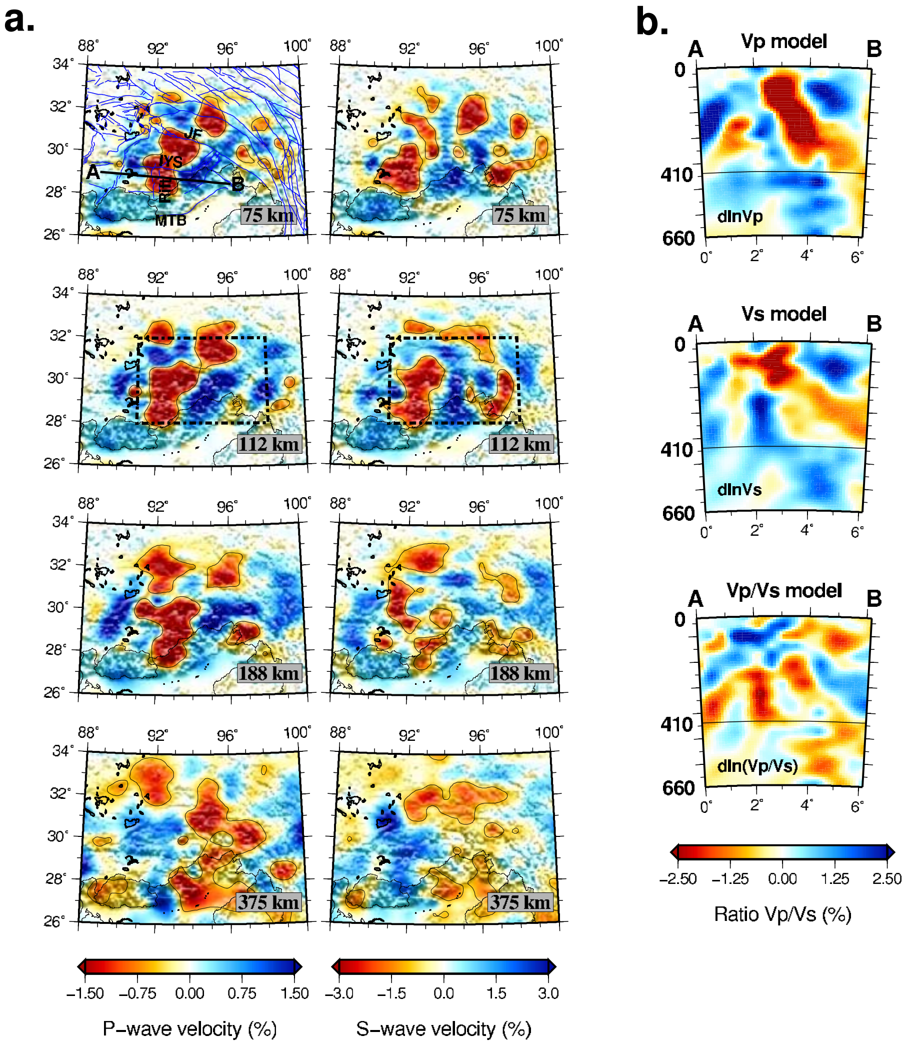

Figure 7. (a) P and S wave velocity perturbations ($dlnV_P$ and $dlnV_S$) relative to the reference model (CRUST2.0 and iasp91) at different depths: 75 km, 112 km, 188 km, and 375 km. The rectangle with dashed lines marks the area which we consider well resolved (also see Figures 4a and 5a). (b) Cross section A-B through P and S wave tomographic models, along the Indus-Yarlung suture and across the rift in southeastern Tibet.

deviations of the difference between the input and output models are respectively 0.7% and 1.3% for the P and S models. This means that about 65% of the amplitudes of the input models at these scales can be recovered. For the case in which the size of the input anomalies is ~100 km × 100 km, the recovery in amplitude is about 55% in the upper 300 km and degrades gradually at greater depths.

5. Results and Discussions

[14] Figure 7a shows P and S wave velocity structures in the crust and upper mantle beneath southeastern Tibet at four different depths. There is a prominent north–south trending, low-velocity structure at ~92° longitude from the lower crust to ~300 km depth. This structure is observed on both the P and S velocity models. It extends across the Indus-Yarlung Suture and coincides strikingly well with a rift on the surface. The shallow (75 km and 112 km) velocity structure (Figure 7a) is in agreement with Pn wave tomography [*Liang and Song*, 2006], which also shows a north–south trending, low-velocity anomaly in the same region, albeit at a coarse resolution and centered somewhat west of the low-velocity feature in this study. At depth above 250 km, there is a high-velocity anomaly east of the north–south trending, low-velocity feature and north of the surface trace of the main boundary thrust fault (MBTF) between the Indian and Eurasian plates. We associate this high-velocity anomaly to the Indian lithosphere underthrusting beneath the plateau. While we agree with the interpretation of Pn tomography that the Indian lithosphere advances further north near the eastern corner than to the west [*Liang and Song*, 2006], the high-velocity anomaly associated with the Indian lithosphere appears to be bounded by the Jiali fault. There is no evidence for a subducted Indian lithosphere at depths greater than 250 km beneath the study area.

[15] West of the north–south trending, low-velocity anomaly is a high-dipping-angle, high-velocity anomaly

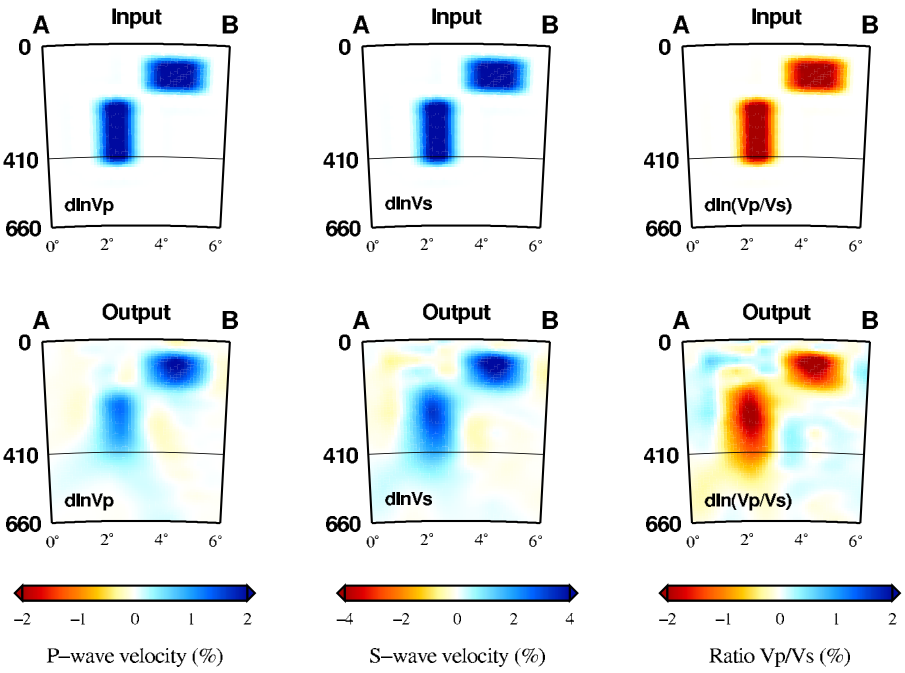

Figure 8. Resolution tests using tabular structures. The cross section A-B is the same as that in the models presented in Figure 7b. (top) Input P and S wave velocity models (+2% and +4%, respectively) and the corresponding V_P/V_S ratio (−2%). The V_P/V_S ratio is obtained by adding the V_P and V_S perturbations from the inversions to the P and S reference models, dividing the perturbed P and S velocities, subtracting the reference V_P/V_S, and then calculating the V_P/V_S change in percentage. (bottom) Retrieved P and S wave velocity models and the corresponding V_P/V_S ratio.

that extends into the upper mantle transition zone, as shown on the cross sections in Figure 7b. Resolution tests using synthetic slabs with a thickness of ~120 km, placed either in the upper and lower parts of the upper mantle, show little vertical smearing in the recovered structures (Figure 8). We conclude that the observed high-velocity anomaly is a robust feature. This anomalous structure is also more or less tabular as opposed to cylindrical. The possible causes for seismic velocity anomalies in the mantle are variations in temperature, chemical composition, and volatile contents. Thermal variations alone cannot fully account for the observed high-velocity anomaly, which coincides with a low V_P/V_S ratio (Figure 7b). A temperature reduction of 400° C for a wide range of upper mantle compositions causes approximately a −0.5% change in V_P/V_S [*Hacker and Abers*, 2004; *Boyd et al.*, 2004], much smaller than the observed anomaly (−1.5%). Resolution tests show that for features comparable to the interpreted, delaminated mantle lithosphere and the Indian mantle lithosphere beneath the eastern indentor, the inversion yields well-recovered V_P/V_S ratios, with magnitudes slightly less than those of the input anomalies (Figure 8). So the magnitude of the real V_P/V_S ratio of the high-angle, high-velocity anomaly is likely greater than the observed value in Figure 7b, requiring a compositional change, which could be accounted for by a refractory mantle depleted of volatiles [*Hacker and Abers*, 2004; *Boyd et al.*, 2004]. The fact that the high-velocity anomaly in the shallow mantle beneath the eastern indentor, which we identify as the Indian mantle lithosphere, also has a low V_P/V_S of a similar magnitude supports the interpretation that the high-dipping-angle, high-velocity anomaly is a sunken mantle lithosphere. The north–south orientation of this feature excludes the possibility that it is a detached Indian plate. We suggest that the low-velocity anomaly immediately east of and above this high-velocity feature represents the mantle asthenosphere that filled the void left by the sunken Eurasian mantle lithosphere (Figure 9). The tabular nature of the high-angle, high-velocity anomaly, the asymmetry of the low-velocity anomaly above it and the rise of this low-velocity anomaly to the base of the crust at ~70 km suggest a process in which the entire mantle lithosphere peeled off as opposed to a partial removal of the mantle from the base of a thickened lithosphere by viscous flow. The shallow asthenosphere and associated heating and weakening of the overlying crust could thus initiate and localize the rifts observed on the surface of the Tibetan Plateau, at least in the region of the Eastern Himalayan Syntaxis.

[16] Roughly coincident with the onset of the east–west extension, potassic volcanism became widespread on the Tibetan Plateau. In southern Tibet, volcanism may have started slightly earlier (~16–20 Ma) and then ceased around 10 Ma [*Williams et al.*, 2004]. The small magnitude of the east–west extension is insufficient to cause decompressional melting of the asthenosphere [*McKenzie and Bickle*, 1988]. Geochemical modeling shows that the magmas in southern Tibet were derived from a small degree (<2%) of partial melting of metasomatized (phlogopite) peridotite in the spinel stability field (at depths of 65–80 km) [*Williams et al.*, 2004]. Our tomographic results are consistent with the geochemical analysis. The delamination of the mantle lithosphere brought the subcontinental mantle

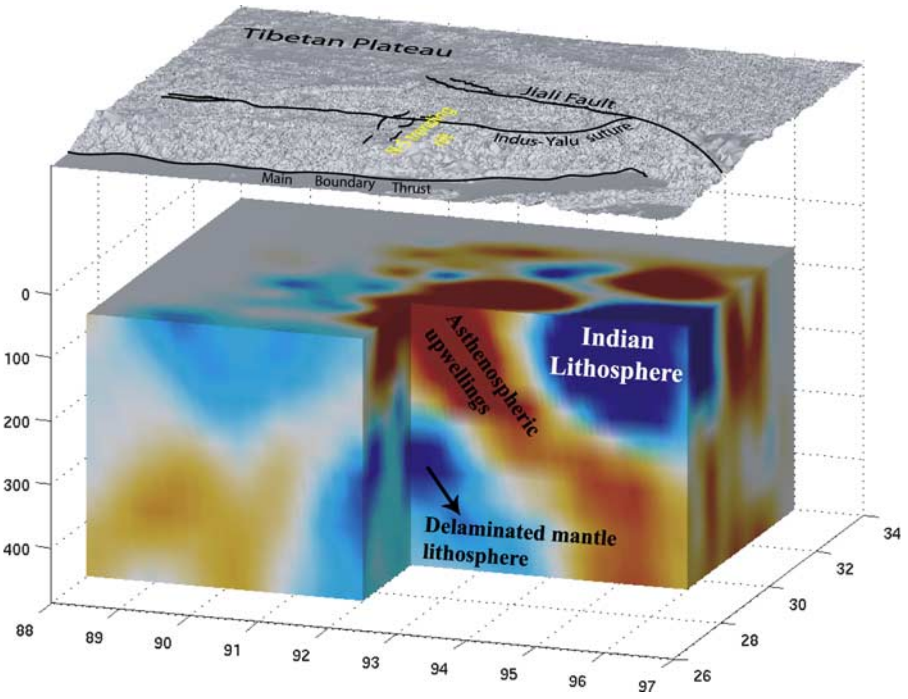

Figure 9. Three-dimensional image of the P wave velocity model with our interpretation of the observed structures. The topography is not to scale.

lithosphere into direct contact with asthenospheric temperatures, so that metasomatized peridotite, which has a lower solidus, underwent partial melting right beneath the crust or released its volatiles into the shallower mantle. The tabular geometry of the north–south trending low-velocity anomaly suggests that the release of volatiles from the sunken mantle lithosphere may contribute significantly to the velocity reduction above it since a buoyant and low-viscosity upwelling tends to form a cylindrical not tabular anomaly. Melting would cease or be greatly reduced once the volatiles in the peridotite are depleted by the melting process. The fact that extension postdates the earliest magmatism by a few million years [*Williams et al.*, 2004] further suggests a causal relationship between the mantle processes and the surface rifts.

[17] The thickening and deformation of the lithosphere caused by the Indo-Eurasia collision is certainly a likely geological setting for the initiation of the lithospheric delamination [*Bird*, 1979], though the exact mechanism for the initiation of the delamination of the mantle lithosphere is unclear. Shear heating through viscous dissipation in the lithosphere likely plays a role in weakening the lithosphere [*Kincaid and Silver*, 1996; *Schott et al.*, 2000] and the initiation of the delamination at a localized shear zone. Numerical simulations on the dynamics of the mantle lithosphere show that mantle delamination and detachment likely occur if the lithosphere is substantially thickened and that the process is strongly controlled by the rheology of the lower crust [*Schott and Schmeling*, 1998; *Morency and Doin*, 2004]. These experiments show that a low-viscosity and hot lower crust favors especially the delamination phenomenon in a thickened lithosphere and the Tibetan Plateau fulfils well these conditions. Several recent Himalayan-Tibetan tectonic investigations have proposed a weak middle-lower crust, which allows crustal flow, to explain the building of the southeastern margin of the Tibetan Plateau [*Clark and Royden*, 2000; *Beaumont et al.*, 2001; *Schoenbohm et al.*, 2006]. This idea is supported by results from geophysical studies that show evidence for localized partial melt within the middle crust in Tibet [*Kind et al.*, 1996; *Wei et al.*, 2001] and a radial anisotropy that can be caused by channel flow within the mid-to-lower Tibetan crust [*Shapiro et al.*, 2004]. However, contrary to the notion that the north–south rift zones in the Tibetan Plateau are shallow features, formed by the eastward motion of the shallow crust that are decoupled from the mantle lithosphere by a low-viscosity lower crust, our results suggest an upper mantle origin of the rift zones, at least in southeastern Tibet, where mantle lithosphere delamination plays a key role in the process of the rise of the plateau.

6. Conclusion

[18] Finite frequency tomography of teleseismic P and S traveltimes shows the presence of a low-velocity anomaly in the crust and upper mantle down to ∼300 km depth beneath a north–south trending rift zone in southeastern Tibet. This low-velocity anomaly is situated above a tabular, high-dipping-angle, high-velocity anomaly that extends into the upper mantle transition zone. The V_P/V_S ratio of this high-velocity anomaly suggests that temperature variations are not the only cause and a highly melt-depleted mantle is required. These results provide evidence for the mantle lithosphere delamination and its link to north–south trending rifts in southeastern Tibet. Studies on an extended region in southern Tibet are thus needed to understand whether this phenomenon is limited to the study area or occurs in a broad region where mantle lithosphere delam-

ination plays an important role in the elevation and deformation of the Tibetan Plateau.

[19] **Acknowledgments.** The data used in this work were obtained from the Incorporated Research Institution for Seismology Data Management Center. We thank the participants in the Namcha Barwa seismic experiments and the Bhutan experiment for making their data available. We thank the reviewers, Peter Molnar and Thomas Hearn, and the Associate Editor, Johannes Weertman, for their helpful reviews, which improve the manuscript. Most figures in this paper were made with General Mapping Tools (P. Wessel and W. H. F. Smith).

References

Armijo, R., P. Tapponnier, J. P. Mercier, and T. Han (1986), Quaternary extension in southern Tibet, *J. Geophys. Res.*, *91*, 13,803–13,872.

Armijo, R., P. Tapponnier, and T. Han (1989), Late Cenozoic right-lateral strike-slip faulting across southern Tibet, *J. Geophys. Res.*, *94*, 2787–2838.

Bassin, C., G. Laske, and G. Masters (2000), The current limits of resolution for surface wave tomography in North America, *Eos Trans. AGU*, *81*(48), Fall Meet. Suppl., Abstract S12A-03.

Beaumont, C., R. A. Jamiesont, M. H. Nguyen, and B. Lee (2001), Himalayan tectonics explained by extrusion of a low-viscosity crustal channel coupled to focused surface denudation, *Nature*, *414*, 738–742.

Bird, P. (1979), Continental delamination and the Colorado Plateau, *J. Geophys. Res.*, *84*, 7561–7571.

Bird, P. (1991), Lateral extrusion of lower crust from under high topography in the isostatic limit, *J. Geophys. Res.*, *96*, 10,275–10,286.

Blisniuk, P. M., B. R. Hacker, J. Glodny, L. Ratschbacher, S. Bi, Z. Wu, M. O. McWilliams, and A. Calvert (2001), Normal faulting in central Tibet since at least 13.5 Myr ago, *Nature*, *412*, 628–632.

Boyd, O. S., C. H. Jones, and A. Sheehan (2004), Foundering lithosphere imaged beneath the southern Sierra Nevada, California, USA, *Science*, *305*, 660–662.

Chen, W. P., and H. Kao (1996), Seismotectonics of Asia: Some recent progress, in *The Tectonics of Asia*, edited by A. Yin and T. M. Harrison, pp. 37–52, Cambridge Univ. Press, New York.

Chen, W.-P., and Z. Yang (2004), Earthquakes beneath the Himalayas and Tibet: Evidence for strong lithospheric mantle, *Science*, *304*, 1949–1952.

Clark, M. K., and L. H. Royden (2000), Topographic ooze: Building the eastern margin of Tibet by lower crustal flow, *Geology*, *28*(8), 703–706.

Coleman, M., and K. Hodges (1995), Evidence for Tibetan Plateau uplift before 14 My ago from a new minimum age for east–west extension, *Nature*, *374*, 49–52.

Conrad, C. P. (2000), Convective instability of thickening mantle lithosphere, *Geophys. J. Int.*, *143*, 52–70.

Dahlen, F. A., S.-H. Hung, and G. Nolet (2000), Fréchet kernels for finite-frequency traveltimes–I. Theory, *Geophys. J. Int.*, *141*, 157–174.

Davaille, A., and C. Jaupart (1993), Transient high-Rayleigh-number thermal convection with large viscosity variations, *J. Fluid Mech.*, *253*, 141–166.

Dewey, J. F. (1988), Extensional collapse of orogens, *Tectonics*, *7*, 1123–1139.

England, P., and G. Houseman (1986), Finite strain calculations of continental deformation: 2. Comparison with the India-Asia collision zone, *J. Geophys. Res.*, *91*, 3664–3676.

England, P., and G. Houseman (1989), Extension during continental convergence, with application to theTibetan Plateau, *J. Geophys. Res.*, *94*, 17,561–17,579.

Hacker, B. R., and G. A. Abers (2004), Subduction Factory 3: An Excel worksheet and macro for calculating the densities, seismic wave speeds, and H_2O contents of minerals and rocks at pressure and temperature, *Geochem. Geophys. Geosyst.*, *5*, Q01005, doi:10.1029/2003GC000614.

Harrison, T. M., P. Copeland, W. S. F. Kidd, and A. Yin (1992), Raising Tibet, *Science*, *255*, 1663–1670.

Harrison, T. M., P. Copeland, W. S. F. Kidd, and O. M. Lovera (1995), Activation of the Nyainqentanghla shear zone: Implications for uplift of the southern Tibetan plateau, *Tectonics*, *14*, 658–676.

Holt, W. E. (2000), Correlated crust and mantle strain fields in Tibet, *Geology*, *28*, 67–70.

Houseman, G. A., E. A. Neil, and M. D. Kohler (2000), Lithospheric instability beneath the Transverse Ranges of California, *J. Geophys. Res.*, *105*, 16,237–16,250.

Hung, S.-H., Y. Shen, and L.-Y. Chiao (2004), Imaging seismic velocity structure beneath the Iceland hot spot: A finite frequency approach, *J. Geophys. Res.*, *109*, B08305, doi:10.1029/2003JB002889.

Jiménez-Munt, I., and J. P. Platt (2006), Influence of mantle dynamics on the topographic evolution of the Tibetan Plateau: Results from numerical modeling, *Tectonics*, *25*, TC6002, doi:10.1029/2006TC001963.

Kapp, P., and J. H. Guynn (2004), Indian Punch Rifts Tibet, *Geology*, *32*, 993–996.

Kincaid, C., and P. Silver (1996), The role of viscous dissipation in the orogenic process, *Earth Planet. Sci. Lett.*, *142*, 271–288.

Kind, R., J. Ni, W. Zhao, J. Wu, X. Yuan, L. Zhao, E. Sandvol, C. Reese, and J. Nabelek (1996), Evidence from earthquake data for a partially molten crustal layer in southern tibet, *Science*, *274*, 1692–1694.

Kind, R., X. Yuan, J. Saul, D. Nelson, S. V. Sobolev, J. Mechie, W. Zhao, G. Kosarev, J. Ni, U. Achauer, and M. Jiang (2002), Seismic images of crust and upper mantle beneath Tibet: Evidence for Eurasian plate subduction, *Science*, *298*, 1219–1221.

Liang, C., and X. Song (2006), A low velocity belt beneath northern and eastern Tibetan Plateau from Pn tomography, *Geophys. Res. Lett.*, *33*, L22306, doi:10.1029/2006GL027926.

Liu, M., and Y. Yang (2003), Extensional collapse of the Tibetan Plateau: Results of three-dimensional finite element modeling, *J. Geophys. Res.*, *108*(B8), 2361, doi:10.1029/2002JB002248.

McCaffery, R., and J. Nabelek (1998), Role of oblique convergence in the active deformation of the Himalayas and southern Tibet Plateau, *Geology*, *26*, 691–694.

McKenzie, D. P., and M. J. Bickle (1988), The volume and composition of melt generation by extension of the lithosphere, *J. Petrol.*, *29*, 625–679.

Mercier, J. L., R. Armijo, P. Tapponnier, E. Carey-Gailhardis, and T.-L. Han (1987), Change from late Tertiary compression to Quaternary extension in southern Tibet during the India-Asia collision, *Tectonics*, *6*, 275–304.

Molnar, P., and P. Tapponnier (1978), Active tectonics of Tibet, *J. Geophys. Res.*, *83*, 5361–5375.

Molnar, P., P. England, and J. Martinod (1993), Mantle dynamics, uplift of the Tibetan Plateau, and the Indian monsoon, *Rev. Geophys.*, *31*(4), 357–396.

Morency, C., and M.-P. Doin (2004), Numerical simulations of the mantle lithosphere delamination, *J. Geophys. Res.*, *109*, B03410, doi:10.1029/2003JB002414.

Morency, C., M.-P. Doin, and C. Dumoulin (2002), Convective destabilization of a thickened continental lithosphere, *Earth Planet. Sci. Lett.*, *202*, 303–320.

Paige, C. C., and M. A. Saunders (1982a), LSQR: An algorithm for sparse linear equations and sparse least squares, *Trans. Math. Software*, *8*, 71–83.

Paige, C. C., and M. A. Saunders (1982b), ALGORITHM 583 LSQR: Sparse linear equations and sparse least squares problems, *Trans. Math. Software*, *8*, 195–209.

Rothery, D. A., and S. A. Drury (1984), The neotectonics of the Tibetan plateau, *Tectonics*, *3*, 19–26.

Royden, L. H. (1996), Coupling and decoupling of crust and mantle in convergent orogens: Implications for strain partitioning in the crust, *J. Geophys. Res.*, *101*, 17,679–17,705.

Schoenbohm, L. M., B. C. Burchfiel, and L. Chen (2006), Propagation of surface uplift, lower crustal flow, and Cenozoic tectonics of the southeast margin of the Tibetan Plateau, *Geology*, *34*(10), 813–816.

Schott, B., and H. Schmeling (1998), Delamination and detachment of a lithospheric root, *Tectonophysics*, *296*, 225–247.

Schott, B., D. A. Yuen, and H. Schmeling (2000), The significance of shear heating in continental delamination, *Phys. Earth Planet. Inter.*, *118*, 273–290.

Shapiro, N. M., M. H. Ritzwoller, P. Molnar, and V. Levin (2004), Thinning and flow of Tibetan crust constrained by seismic anisotropy, *Science*, *305*, 233–236.

Sol, S., et al. (2007), Geodynamics of the southeastern Tibetan Plateau from seimic anisotropy and geodesy, *Geology*, *35*(6), 563–566.

Tapponnier, P., J. L. Mercier, R. Armijo, T. Han, and J. Zhao (1981), Field evidence for active normal faulting in Tibet, *Nature*, *294*, 410–414.

Tapponnier, P., G. Peltzer, A. Y. Le Dain, R. Armijo, and P. Cobbold (1982), Propagating extrusion tectonics in Asia: New insights from simple experiments with plasticines, *Geology*, *10*, 611–616.

Tapponnier, P., Z. Xu, F. Roger, B. Meyer, N. Arnaud, G. Wittlinger, and J. Yang (2001), Oblique stepwise rise and growth of the Tibet Plateau, *Science*, *294*, 1671–1677.

VanDecar, J. C., and R. S. Crosson (1990), Determination of teleseismic relative phase arrival times using multi-channel cross-correlation and least squares, *Bull. Seismol. Soc. Am.*, *80*, 150–169.

Wei, W., et al. (2001), Detection of widespread fluids in the Tibetan crust by magnetotelluric studies, *Science*, *292*, 716–718.

Williams, H. M., S. P. Turner, J. A. Pearce, S. P. Kelley, and N. B. W. Harris (2004), Nature of the source regions for post-collisional, potassic magmatism in southern and northern Tibet from geochemical variations and inverse trace element modeling, *J. Petrol.*, *45*, 555–607.

Yang, T., Y. Shen, S. van der Lee, S. C. Solomon, and S.-H. Hung (2006), Upper mantle structure beneath the Azores hotspot from finite-frequency seismic tomography, *Earth Planet. Sci. Lett.*, *250*, 11–26.

Yin, A. (2000), Mode of Cenozoic east–west extension in Tibet suggesting a common origin of rifts in Asia during the Indo-Asian collision, *J. Geophys. Res.*, *105*(B9), 21,745–21,759.

Yin, A., and T. M. Harrison (2000), Geologic evolution of the Himalayan-Tibetan orogen, *Annu. Rev. Earth Planet. Sci.*, *28*, 211–280.

Yin, A., T. M. Harrison, F. J. Ryerson, W. J. Chen, W. S. F. Kidd, and P. Copeland (1994), Tertiary structural evolution of the Gangdese thrust system in southeastern Tibet, *J. Geophys. Res.*, *99*, 18,175–18,201.

Zhao, W. L., and W. J. Morgan (1987), Injection of Indian crust into Tibetan lower crust: A two-dimensional finite element model study, *Tectonics*, *6*, 489–504.

Y. Ren and Y. Shen, Graduate School of Oceanography, University of Rhode Island, South Ferry Road, Narragansett, RI 02882, USA. (ren@gso.uri.edu; yshen@gso.uri.edu)